2008

Observed structure, evolution and potential intensity of category 5 hurricane Isabel

Bell, M. M

Observed Structure, Evolution, and Potential Intensity of Category 5 Hurricane Isabel (2003) from 12 to 14 September

MICHAEL M. BELL*

National Center for Atmospheric Research,+ Boulder, and Colorado State University, Fort Collins, Colorado

MICHAEL T. MONTGOMERY

Department of Meteorology, Naval Postgraduate School, Monterey, California, and NOAA/Hurricane Research Division, Miami, Florida

(Manuscript received 14 April 2006, in final form 21 June 2007)

ABSTRACT

Unprecedented observations of Hurricane Isabel (2003) at category 5 intensity were collected from 12 to 14 September. This study presents a detailed analysis of the inner-core structure, atmospheric boundary layer, sea surface temperature, and outflow layer of a superintense tropical cyclone using high-resolution in situ flight-level, NCAR GPS dropwindsonde, Doppler radar, and satellite measurements. The analysis of the dropwindsonde and in situ data includes a comprehensive discussion of the uncertainties associated with this observational dataset and provides an estimate of the storm-relative axisymmetric inner-core structure using Barnes objective analysis. An assessment of gradient and thermal wind balance in the inner core is also presented. The axisymmetric data composites presented in this study suggest that Isabel built a reservoir of high moist entropy air by sea-to-air latent heat flux inside the low-level eye that was utilized as an additional energy source to nearly maintain its extreme intensity even after crossing the cool wake of Hurricane Fabian. It is argued here that the combined mean and asymmetric eddy flux of high moist entropy air from the low-level eye into the eyewall represents an additional power source or "turbo boost" to the hurricane heat engine. Recent estimates of the ratio of sea-to-air enthalpy and momentum exchange at high wind speeds are used to suggest that Isabel utilized this extra power to exceed the previously assumed intensity upper bound for the given environmental conditions on all three days. This discrepancy between a priori potential intensity theory and observations may be as high as 35 m s^{-1} on 13 September.

1. Introduction

Category 5 and supertyphoon-class tropical cyclones[1] (TCs) are some of the most awe-inspiring natural phenomena on the planet. Their savage beauty and tremendous power have had profound impacts on history (Emanuel 2005), and these relatively rare phenomena have the potential damage value of 500 times that of a category 1 storm (Pielke and Landsea 1998). Meteorological observations from storms that achieve this infamous status provide a glimpse of the hurricane heat engine operating at peak efficiency, yielding new insights into the dynamics and thermodynamics of TCs.

One goal toward reaching a complete understanding of hurricane intensity is developing an accurate theory that predicts a reasonable upper limit, or the potential intensity (PI), of a TC for a given set of environmental conditions. PI theory not only provides a prediction of

* Current affiliation: National Center for Atmospheric Research, Boulder, Colorado, and Naval Postgraduate School, Monterey, California.

+ The National Center for Atmospheric Research is sponsored by the National Science Foundation.

Corresponding author address: Michael Bell, National Center for Atmospheric Research, P.O. Box 3000, Boulder, CO 80307. E-mail: mbell@ucar.edu

DOI: 10.1175/2007MWR1858.1

[1] Category 5 refers to the highest level on the Saffir–Simpson scale in the Atlantic basin, while supertyphoon is a term used for intense typhoons in the western Pacific basin. They are defined by maximum sustained 1-min surface winds greater than 135 and 130 kt, respectively.

the capability for a storm to achieve category 5, but also a simplified framework in which to study the processes that compose the hurricane engine. Understanding intensity change then becomes a matter of accurately determining the limiting factors that prevent a TC from realizing and/or maintaining its peak intensity and efficiency.

One approach to PI is to use statistical predictors, such as the work of DeMaria and Kaplan (1994). As a testament to the difficulty in forecasting TC intensity, statistical models currently show more skill than operational dynamical models (DeMaria et al. 2005). Statistical PI provides an important empirical upper limit for intensity and verification of the importance of environmental parameters that are favorable for development, but it has little to say about the processes that control TC intensity. In an effort to understand these fundamental mechanisms, several other approaches have been taken over the last few decades to predict the PI based on simplifications of the energetics and dynamics of the atmosphere–ocean system. These theories should be valid for a range of environmental conditions, and significant violations of the predicted PI beyond observational error are therefore not statistical anomalies, but indications that the dynamical basis of the theory is either flawed or incomplete.

Predictions for the minimum surface pressure using a parcel approach were first developed by Miller (1958). The surface pressure was obtained through two hydrostatic integrations: by first lifting an air parcel moist adiabatically in the eyewall, and subsequently sinking dry adiabatically (with mixing from the eyewall) in the eye. Holland (1997) modified this theory by incorporating the pressure dependence of moist entropy and reducing the surface pressure in the eyewall integration iteratively until the solution converged. Neither of these two approaches explicitly considered heat and momentum transfer between the atmosphere and ocean. In contrast, heat and momentum transfer plays a primary role in theories proposed by Kleinschmidt (1951), Malkus and Riehl (1960), and Emanuel and colleagues (Rotunno and Emanuel 1987; Emanuel 1986, 1988, 1991, 1995, 1997; Bister and Emanuel 1998; Emanuel et al. 2004; this theoretical work is hereinafter collectively referred to as EPI). We have focused this paper on comparisons with EPI theory since air–sea heat and momentum fluxes are not explicitly included in Miller's (1958) or Holland's (1997) PI theories, nor do these theories offer predictions for maximum sustained tangential wind (V_{max}). Camp (1999) and Camp and Montgomery (2001) provide a more comprehensive review of PI theory for interested readers.

Previous studies have tested various PI theories using numerical models (Rotunno and Emanuel 1987; Persing and Montgomery 2003, hereinafter PM03), east Pacific Ocean environmental soundings (Hobgood 2003), and best-track and satellite datasets (Tonkin et al. 2000). PM03 performed a rigorous test of EPI theory with the axisymmetric numerical model developed by Rotunno and Emanuel (1987) and found that the theoretical PI was exceeded when the resolution of the model was able to resolve the hurricane eye and its interaction with the eyewall. Their work suggested that the low-level eye, traditionally passive in PI theories (e.g., Emanuel 1995), plays an important role in the energetics of the TC engine by providing a reservoir of high moist entropy air that augments the energy available between the outer core and the base of the eyewall. PM03 coined the term "superintensity" to refer to storms that exceeded their PI by utilizing this mechanism.

Comparable tests of PI with observational data are limited. A climatological study of hurricane intensity by Tonkin et al. (2000) showed that both the Emanuel and Holland PI theories demonstrated reasonable predictive capability for all ocean basins and seasons, with a general tendency for overestimation of the intensity. Given the wide range of adverse environmental conditions a tropical cyclone might encounter, this result is perhaps not too surprising. However, an interesting subset of storms was found that exceeded their PI. Their study showed a broad range of SSTs for which both PI models underestimated the TC intensity. Whether this is due to the use of climatological sea surface temperature (SST), satellite-based intensity estimates, or a flawed theory is not known. More detailed observations are therefore needed to elucidate the structure, intensity, and environmental parameters of the anomalous cases.

A critical limitation to testing the limits of PI theory is the lack of detailed observations of the inner-core kinematic and thermodynamic structure and environmental conditions of category 5 TCs. Even with operational aircraft reconnaissance, it is difficult to establish high-resolution two- or three-dimensional structures of a hurricane (Hawkins and Rubsam 1968; Hawkins and Imbembo 1976; Frank 1984; Jorgensen 1984; LeeJoice 2000).[2] Intensive observing periods (IOPs) conducted as part of a dedicated field project are an effective, and often only, way to obtain the quantity and quality of

[2] Airborne Doppler radars can now provide operational estimates of three-dimensional kinematic and precipitation fields, but high-resolution multidimensional spatial fields of thermodynamic data are still difficult to obtain.

observations needed to adequately test meteorological theory. Three IOPs into Hurricane Isabel were obtained from 12 to 14 September 2003 while it was at category 5 intensity. These IOPs were supported by the National Oceanic and Atmospheric Administration (NOAA) and Office of Naval Research (ONR) as part of the Coupled Boundary Layer Air–Sea Transfer (CBLAST) field campaign, NOAA Hurricane Field Program, and NOAA/National Environmental Satellite, Data, and Information Service (NESDIS) Ocean Winds experiment.

The Isabel dataset provides a unique opportunity to use detailed in situ observations of the inner-core structure, atmospheric boundary layer, sea surface temperature, and outflow layer to test the predictions of Emanuel's PI theory, and examine the structure and balance of the hurricane engine operating at near-peak efficiency. This study will quantify the environmental parameters used in the EPI theory using measurements obtained during the CBLAST field campaign, and compare the resulting maximum intensity predictions with the observed intensity of a category 5 TC. These data are also used to assess the validity of the assumptions of gradient and thermal wind balance invoked in the derivation of the theory. EPI theory predicts an upper bound on the mean tangential wind at the swirling boundary layer top for given environmental conditions. Montgomery et al. (2006, hereafter M06) suggested that Hurricane Isabel surpassed this upper bound on 13 September 2003, providing the first evidence for the existence of superintense storms in nature that were previously predicted using high-resolution computer simulations (PM03). This paper extends this analysis over three consecutive days from 12 to 14 September 2003 and suggests that Isabel was superintense over the entire period.

The in situ fields of pseudoequivalent potential temperature (labeled hereafter θ_e) and radial wind analyzed here suggest that a reservoir of high entropy air was enhanced through sea-to-air latent heat flux in the low-level eye between 12 and 13 December, and that significant penetration of near-surface air from the inflow was enhanced thermodynamically, acquiring the characteristics of the high entropy air in the eye. This low-level inflow replenishes the air transported/mixed out of the eye and provides additional power to the hurricane by injection into the eyewall cloud. The eye dynamics can therefore be figuratively compared to a second cycle or "afterburner" for the Carnot engine, in which thermodynamic energy drawn from the underlying ocean within the eye augments the energy obtained from the ocean underneath and outside the eyewall, where current theory assumes all of the energy uptake occurs (e.g., Emanuel 1995, 1997). It is suggested that the low-level eye was utilized as an additional energy source to nearly maintain its extreme intensity through 14 September, even after crossing the cool wake of Hurricane Fabian.

Section 2 details the dataset and analysis methodology used in this study. The evolution of Isabel's axisymmetric structure from 12 to 14 September is presented in section 3, including what we believe is the highest-resolution potential vorticity fields of the hurricane inner core derived from observational data to date. An analysis of gradient and thermal wind balance is given in section 4. Observed environmental conditions and a summary of EPI predictions are presented in section 5. A summary and conclusions are given in section 6.

2. Dataset and analysis methodology

a. Hurricane Isabel (2003)

Hurricane Isabel became a tropical depression from an African easterly wave at 0000 UTC 6 September 2003 and was quickly named a tropical storm 6 h later (Lawrence et al. 2005). Isabel continued intensification until 11 September, when Dvorak satellite estimates indicated it reached category 5 intensity, with an estimated minimum central pressure of 915 hPa and maximum sustained surface winds of 145 kt. Isabel maintained maximum sustained surface wind speeds above 130 kt and central pressures below 940 hPa in relatively favorable environmental conditions until 15 September, at which point environmental vertical wind shear increased and the storm began to weaken. Isabel made landfall in North Carolina three days later as a large category 2 hurricane. The National Hurricane Center (NHC) best track and intensity are shown in Fig. 1. Two NOAA WP-3Ds (P3s) conducted three IOPs from 12 to 14 September as part of the CBLAST and NOAA/NESDIS Ocean Winds experiments. NHC best-track intensities were estimated at 135–140 kt (category 5) during the ~1600–2300 UTC time period when observations were collected on each day, and an estimated 130 kt at the end of the final IOP on the 14th. The 85-GHz and visible satellite imagery from the three analysis days are shown in Fig. 2. The nearly circular core of deep convection of Isabel, represented by the cold (red) 85-GHz brightness temperatures and asymmetric structures in the low-level stratus clouds in the eye, are evident during all three IOPs. While the magnitude of the asymmetries is generally an order of magnitude smaller than the primary circulation in the inner core (Shapiro and Montgomery 1993; Reasor et al. 2000), the low-level vortex structures evident in the

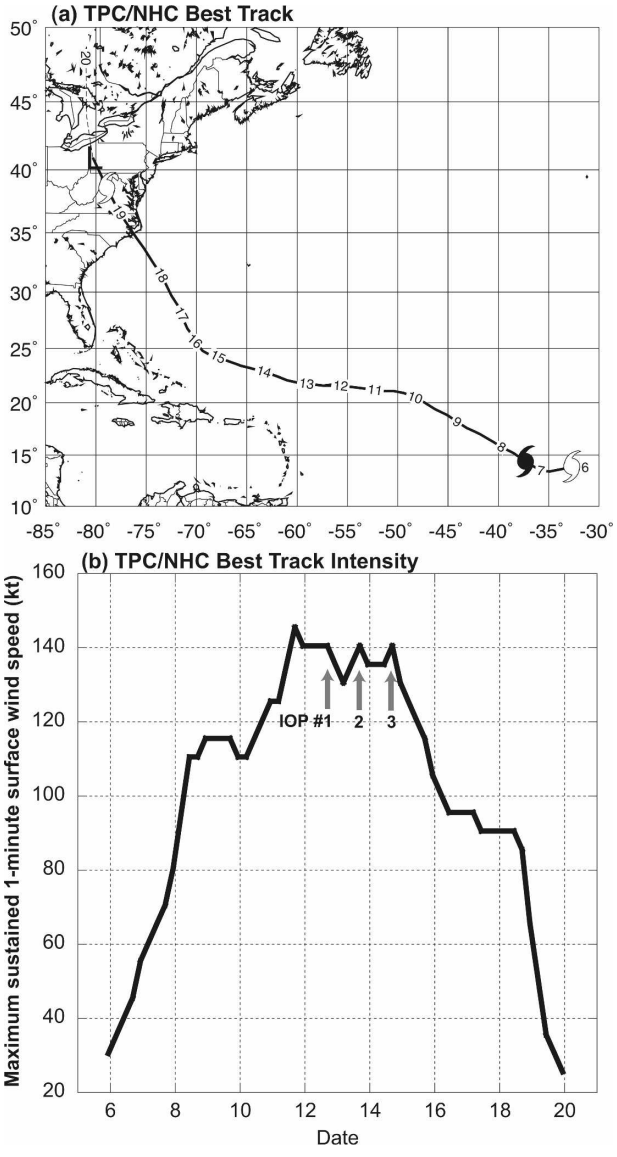

FIG. 1. NOAA Tropical Prediction Center/National Hurricane Center (a) best track and (b) best-track intensity for Hurricane Isabel. Open hurricane symbol indicates tropical storm strength, filled symbol indicates hurricane strength, and "L" indicates extratropical transition. The three intensive observing periods on 12, 13, and 14 Sep are highlighted.

stratus clouds within the eye (Fig. 2, right column) are argued here to be important elements that help to maintain category 5 intensity over these three days.

The NOAA G-IV and U.S. Air Force (USAF) C130 aircraft also collected observations during the IOPs for operational surveillance and reconnaissance. In situ flight-level and dropwindsonde data were collected by all four aircraft, with additional Doppler radar and radiometer data obtained by the P3s only. This study focuses on the in situ, dropwindsonde, and radiometer data, but radar analysis was also performed for independent verification of the large-scale wind fields (not shown) and small-scale features (Aberson et al. 2006). Pseudoequivalent potential temperature was calculated following the empirical formulation in Bolton (1980).[3]

b. *In situ flight-level data*

Flight-level in situ data used in this study were kindly provided by NOAA's Hurricane Research Division. Data were available at 1-s resolution for NOAA aircraft and 10-s resolution for the Air Force C130s. G-IV flight level data were not used, except for dropwindsonde release information. A rudimentary correction for instrument-wetting errors (Zipser et al. 1981; Eastin et al. 2002) was applied to supersaturated dewpoint temperature measurements. This correction assumes that the errors for each sensor are equal in magnitude but opposite in sign and was shown by Eastin et al. (2002) to reduce the majority of significant wetting errors but not remove them completely, resulting in a mean θ_e error of 2.7 K.

c. *NCAR GPS dropwindsondes*

An unprecedented total of 184 National Center for Atmospheric Research (NCAR) global positioning system (GPS) dropwindsondes (sondes) were released into the inner and outer core[4] of Hurricane Isabel during the three CBLAST IOPs. An additional 38 sondes were released in the ambient environment by the NOAA G-IV on 13 and 14 September. This instrument provides pressure, temperature, relative humidity (PTH), and horizontal wind speed at 2-Hz temporal resolution along a Lagrangian trajectory falling between 12 and 15 m s^{-1} in the lower troposphere. This yields a vertical resolution of approximately 5 m, with typical PTH errors less than 1.0 hPa, 0.2°C, and 5% respectively, and wind errors less than 2.0 m s^{-1} (Hock and Franklin 1999). Vertical velocity was obtained from the dropwindsondes by removing the estimated termi-

[3] Strictly speaking, EPI theory is derived using reversible thermodynamics. Because of the lack of liquid water measurements from the dropwindsonde data, a pseudoequivalent potential temperature is used throughout this study. Comparisons including liquid water measurements from the Johnson–Williams liquid water probe at the 700-hPa flight level indicate that this approximation leads to a linear discrepancy between the reversible and pseudoequivalent temperatures of ~0.14% per g kg^{-1} of total water mixing ratio. This indicates pseudoequivalent potential temperature is ~11 K larger at ~20 g kg^{-1}.

[4] Inner-core observations are defined in this paper as <60-km radius from the center, outer core as 150–250-km radius.

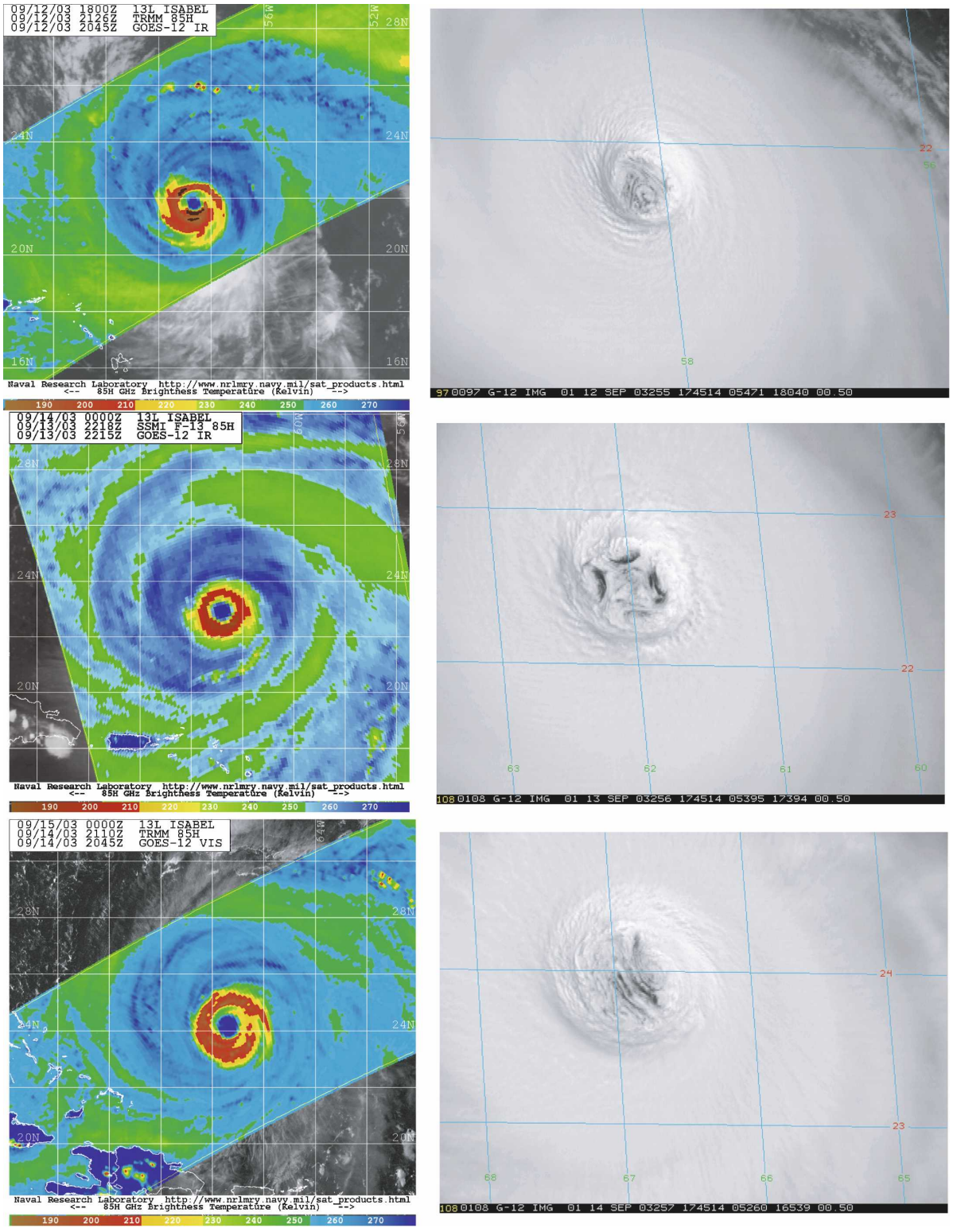

FIG. 2. (left) Satellite appearance of Hurricane Isabel at 85 GHz (courtesy NRL/Monterey) and (right) visible (courtesy CIRA/CSU) wavelengths during each IOP. The 85-GHz imagery is from (a) TMI at 2126 UTC 12 Sep, (c) SSM/I at 2218 UTC 13 Sep, and (e) TMI at 2110 UTC 14 Sep. Visible images are from GOES super-rapid-scan operations at 1745 UTC on each day.

nal fall speed of the sondes as a function of pressure. This technique has been shown to be relatively robust for mesoscale vertical motions in hurricanes, with an estimated error of 0.5–1.0 m s^{-1} (Franklin et al. 2003).

All dropwindsondes were quality controlled to remove noise and other instrument errors with either NCAR Aspen or NOAA/Hurricane Research Division (HRD) Editsonde software. For this study, all NOAA-released sondes and most USAF sondes were kindly processed by HRD using Editsonde, with some additional USAF sondes processed by the authors using Aspen. Even though both of these programs are based on the same quality control algorithms, tests were performed to determine the differences, if any, between the two software packages. Though individual processed results occasionally exhibited some differences, only minor discrepancies were found in the resulting axisymmetric composites after averaging the large number of data points.

The relative humidity for a particular set of dropwindsondes released from the NOAA 43 P3 aircraft was problematic, however, reaching only ~85% RH in the eyewall, with values as low as 65%. Since the theoretical value in precipitation and thick marine stratocumulus should be near 100%, this suggested a potential dry bias. However, the true homogeneity of the eyewall cloud is unknown, and arbitrary saturation of eyewall profiles was not justified. A scaled RH correction of ~12%–15%, was therefore applied to the affected dropwindsondes (see Bell 2006 for more details). The correction was stable, suggesting that the degree of molecular contamination (Wang 2005) was consistent for that batch of sondes. A few minor RH adjustments were made on some sondes released by NOAA 42 as part of routine quality control. While the applied correction seems plausible, the degree to which the corrected sonde profiles represent the true eyewall RH is still somewhat uncertain. To verify that the analysis was not overly sensitive to the uncertainty of these measurements, two additional composites were constructed without the suspect data and without applying any RH corrections. These led to changes of θ_e in the eyewall of 2–4 K, comparable to the error for uncorrected instrument wetting (Eastin et al. 2002). It is therefore believed that the postprocessing of the relative humidity data removed all major errors, but potential sensor wetting and/or molecular contamination still yield an estimated θ_e uncertainty of ~3 K.

d. Diagnosed TC centers

Cylindrical coordinates allow for the representation of the wind field by tangential and radial components, and structural decomposition into azimuthal harmonics (wavenumbers). This requires accurate center estimates for a meaningful coordinate transformation. The center-finding method of Willoughby and Chelmow (1982, hereafter WC82) relies on both pressure and wind information from high-resolution flight-level data, and has been shown to be accurate to ~3 km. The variable time interval between fixes, variability of the center with height, and local pressure and wind minima associated with mesovortices in the eye makes determining an accurate set of centers for an entire IOP challenging and may increase the center uncertainty. The analyzed set of centers for each day was created by a linear interpolation between selected robust center fixes obtained by the WC82 method using storm-relative winds (i.e., winds with the storm motion vector removed) at 2-km height, with constraints provided by NHC best-track data when reliable center fixes were not available. This yielded a general west-northwesterly storm motion of ~7 m s^{-1} on each day.

Errors in the analysis introduced by center uncertainty were examined by a Monte Carlo approach, perturbing the estimated center to account for center uncertainties resulting from small-scale oscillations, interpolation error, and vortex tilt. This yielded minor differences for reasonable center displacements of up to 5 km. Dropwindsondes released in the eye were examined individually for potential errors in center position, because of the increased sensitivity of the cylindrical coordinate transform at small radii. Given the accuracy of the individual center fixes and relative robustness of axisymmetric quantities to the random perturbation, there appear to be no systematic errors introduced by an estimated <5-km mean center uncertainty.

e. Barnes objective analysis

After quality control and decomposition into storm-relative cylindrical coordinates, the resulting data distribution in the radial–azimuthal and radial–vertical planes for each IOP is shown in Fig. 3. By making the steady-state, axisymmetric assumption, the primarily Eulerian flight level and Lagrangian dropwindsonde measurements can both be treated as axisymmetric, instantaneous snapshots in the radial–vertical plane of the storm circulation. The aircraft or dropwindsonde measurement is then weighted according to its distance from a given storm-relative radius and altitude (grid point). The weighted observations from different azimuths and times are then averaged by the Barnes objective analysis (Barnes 1973; Koch et al. 1983) to yield an estimate of the axisymmetric structure. Whereas the Barnes objective analysis has been used previously in hurricane studies (e.g., Velden et al. 1992; Franklin et

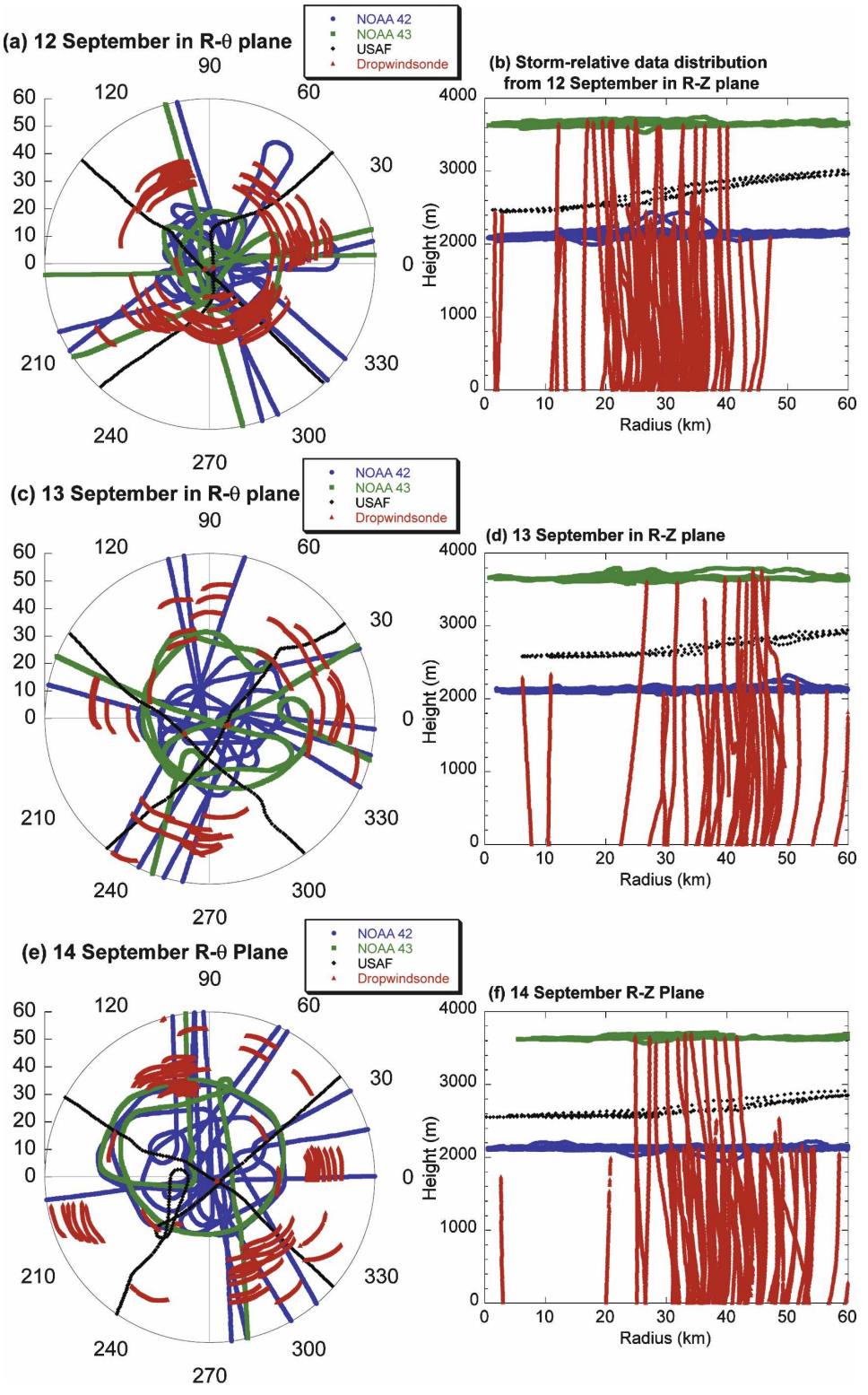

FIG. 3. Dropwindsonde locations and trajectories and aircraft flight tracks relative to storm center from 1600 to 2300 UTC on each day. Storm-relative data distribution in the (left) azimuthal (r–θ) plane and (right) radial–height (r–z) plane, showing the NOAA P-3 (42 in blue, 43 in green), USAF C-130 (in black) flight tracks, and dropwindsonde trajectories (in red). The dropwindsondes in the left column move cyclonically (counterclockwise).

al. 1993), its application for inferring radius–height mean hurricane structure is believed to be novel. A total of ~43 500, 30 700, and 37 800 data points were available on each day from dropwindsonde and flight-level data. The sounding data comprised 63%, 48%, and 59% of the data distributions for each IOP, from 67, 35, and 58 inner-core soundings, respectively. The Barnes analysis procedure used radial and vertical grids of 2500 and 250 m, respectively, to account for the differing horizontal and vertical data resolution and spacing. A minimal gamma smoothing parameter of 0.3 and radial and vertical weight parameters were then set to produce the maximum spectral resolution (10 and 1 km, respectively) allowable for the given grid spacing.

All variables that do not contain derivatives were calculated from the observational data and then composited using the Barnes analysis. Given the relatively dense observations and high spatial resolution of the composite, an attempt was also made to assess kinematic and thermodynamic gradients derived from the composite in the inner core. The vorticity and potential vorticity (which also involves the potential temperature gradient) resulting from these calculations are therefore presented in section 3, with the caveat that some of the detailed structure and exact magnitude may be grid dependent.

Uncertainties arising from undersampling, the location of the circulation center, and dropwindsonde terminal fall speed may produce unbalanced divergence and vertical velocity fields at any particular point, resulting in a nonzero residual in the mass continuity equation. Unfortunately, the resulting calculation was too sensitive to quantitatively determine this residual. The finescale composite-derived gradients of pressure and θ_e in the balance diagnosis (section 4) were suspect, and derivatives were calculated from radially and vertically binned averages instead of the composite data. This technique is believed to more accurately capture the magnitude of the gradients at a specific vertical level, with the cost of decreased radial spatial resolution, which is appropriate for the assessment of balance at the larger storm scale.

3. Axisymmetric structure and evolution from 12 to 14 September

a. Kinematic structure and evolution

This analysis of Hurricane Isabel suggests that despite the relatively steady-state intensity, the storm structure slowly evolved from 12 to 14 September. Figure 4 shows the radius–height composite storm-relative tangential wind (color), radial wind (contour), and secondary circulation (vector) in meters per second. The origin (0, 0) denotes the storm center at the ocean surface. Isabel crossed the cool wake of Fabian on 13 September, resulting in a 1°–2°C reduction in sea surface temperature (see Fig. 9), and one might expect the intensity to have decreased, but this analysis indicates otherwise. The mean peak tangential wind at the radius of maximum wind (RMW) remained very strong on all three days, with the core region of maximum tangential winds decaying from ~80 to 74 m s^{-1}, rising from ~500-m to 1-km altitude, and expanding from ~25- to 50-km radius. The low-level radial inflow increased in both depth and intensity from 12 to 13 September, but then weakened again on 14 September. A persistent region of ~5–10 m s^{-1} outflow just above the boundary layer near the RMW is evident on all three days. The derived vertical velocity is qualitatively consistent with the radial divergence, showing weak vertical motions inside the eye and a maximum updraft nearly collocated with the RMW on each day. Lowest-level (representative of ~100 m) radial inflow of 20 m s^{-1} located at 25-km radius from the center on 13 September suggests significant penetration of air from the eyewall into the eye. This measurement of strong inflow inside the eye appears to be robust (Bell 2006), but because of limited sampling it may not be a quantitatively accurate depiction of the axisymmetric inflow at these radii.

There is the possibility that the expansion of the RMW was associated with an eyewall replacement cycle from 12 to 13 September (Kozich 2006). Radar reflectivity imagery [not shown; reflectivity composites are available from NOAA/Atlantic Oceanographic and Meteorological Laboratory (AOML)/HRD at www.aoml.noaa.gov/hrd] and microwave imagery (Fig. 2a) suggests that an outer rainband began to encircle the primary eyewall late on the 12th. However, only limited flight-level data and microwave imagery between IOPs is available, making it difficult to determine the details of an eyewall replacement and/or expansion. The transition between 12 and 13 September occurred with a ~10-hPa rise in central pressure, and a brief weakening but rapid recovery of the maximum tangential wind speed. A more detailed analysis of this transition is beyond the scope of this study.

b. Equivalent potential temperature and absolute angular momentum

Figure 5 shows the radius–height composite θ_e (color), specific absolute vertical angular momentum (contour), and transverse secondary circulation (vector). The specific absolute vertical angular momentum (absolute circulation) is $M = rv + \frac{1}{2}fr^2$, where r is the radius from the vortex center, v is the storm-relative tangential velocity, and f is the Coriolis parameter.

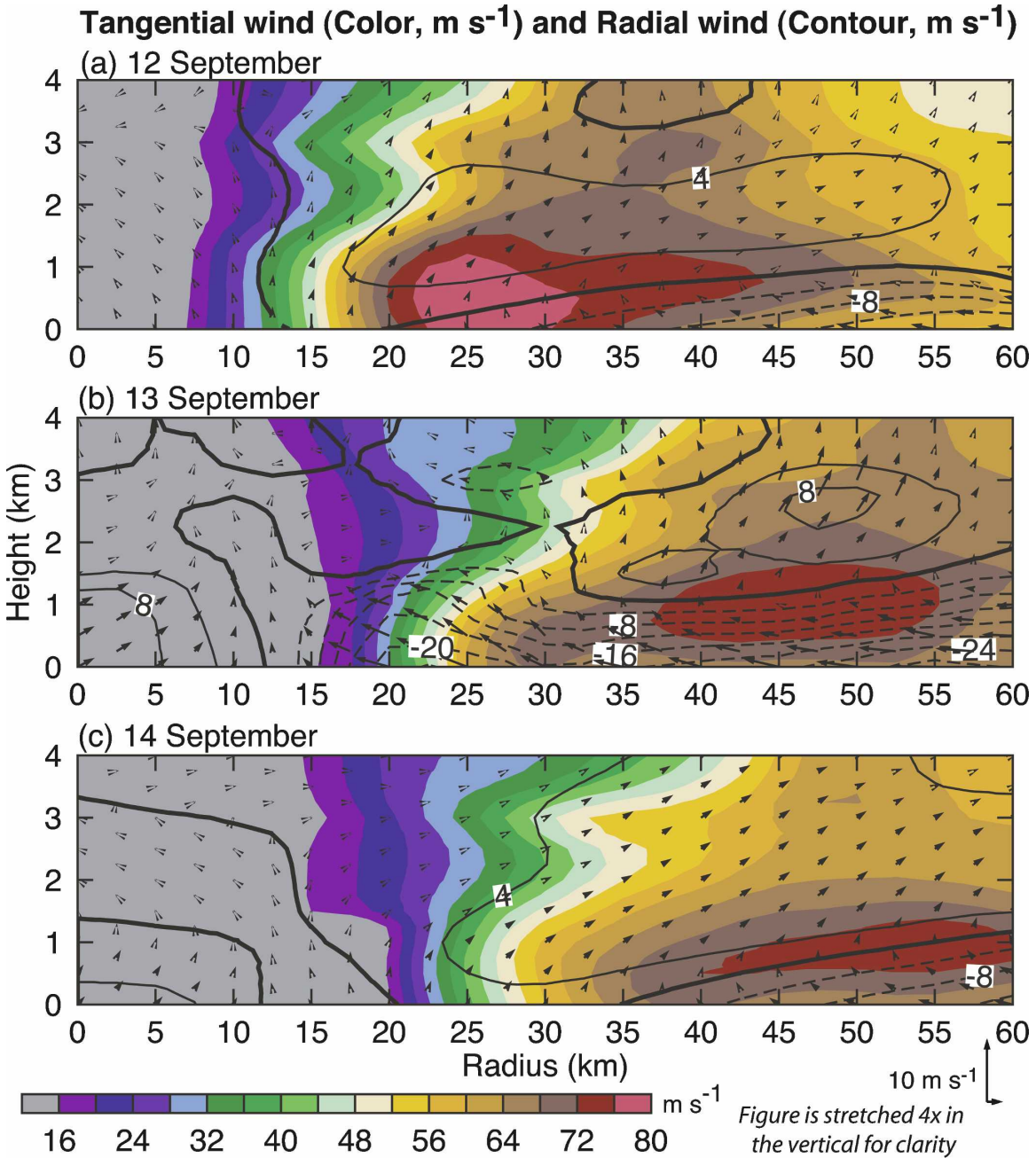

FIG. 4. Radius–height azimuthal mean storm-relative tangential wind (color), radial wind (contour), and the secondary circulation (vector) in m s^{-1} derived from GPS dropwindsonde and flight-level data from (a) 12, (b) 13, and (c) 14 Sep 2003.

Some of the most dramatic changes in the inner-core storm structure are illustrated here, with a distinct increase in the low-level θ_e in the eye from 12 to 13 September, followed by an increase in eyewall θ_e on 14 September. The radial θ_e gradient is generally negative throughout all three days, except for very near the center on the 12th. On the 14th, it appears as if the θ_e has been "mixed out," with relatively lower values found in the eye, and an increase at the eyewall. These figures suggest that there were significant changes in the mean moist entropy structure over these three days. Radial profiles of mean potential temperature and vapor mixing ratio at the lowest composite level are shown in Fig. 6. These radial profiles suggest that the increase in mean θ_e after the 12th was primarily due to increased low-level moisture and occurred despite a rise in central

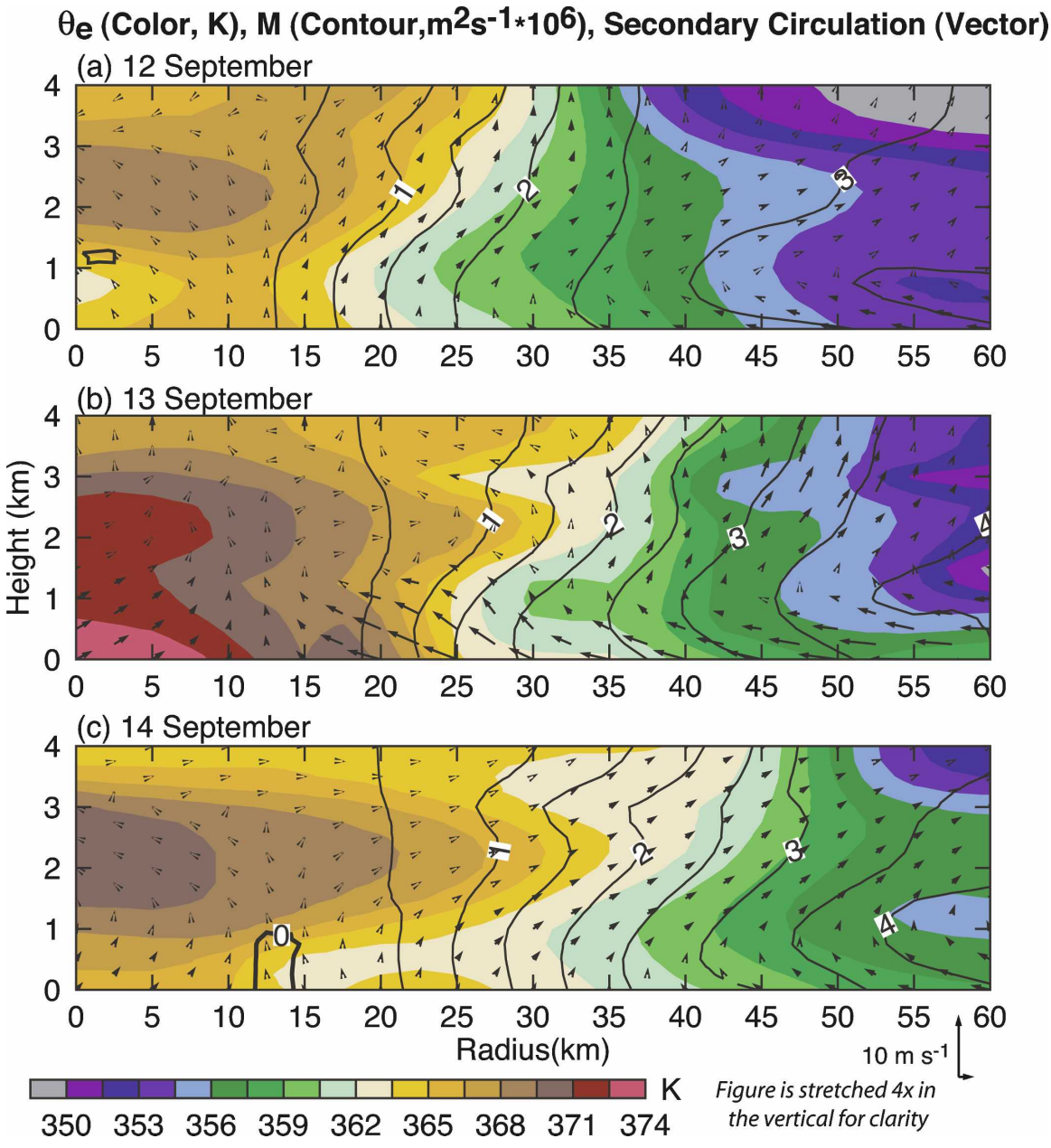

FIG. 5. Radius–height azimuthal mean storm-relative θ_e (color; K); absolute angular momentum (contour; $m^2\ s^{-1} \times 10^6$); and transverse secondary circulation (vector) from (a) 12, (b) 13, and (c) 14 Sep 2003.

pressure of ~10 hPa. This supports the hypothesis of persistent latent heat flux from the underlying ocean inside the low-level eye and possibly radial moisture flux due to mixing from the eyewall. Whereas a detailed calculation of the residence time of air parcels in Isabel's eye is beyond the scope of this study, Cram et al. (2007) showed that residence times in the eye for significant θ_e gain in their numerical simulation of Hurricane Bonnie were commonly on the order of 40–60 min and as low as 15 min. This suggests that latent heat fluxes in the eye can modify inflowing air parcels on even relatively short time scales.

The concurrent increase of the moist entropy, vertical velocity, and radial inflow from 12 to 13 September suggests a positive feedback between these fields. The addition of higher θ_e to the eyewall cloud enhances (locally) buoyant updrafts (Braun 2002; Eastin et al. 2005; Smith et al. 2005), which is believed to support a stronger, deeper radial inflow. This may allow Lagrangian parcels to more easily breach the high in-

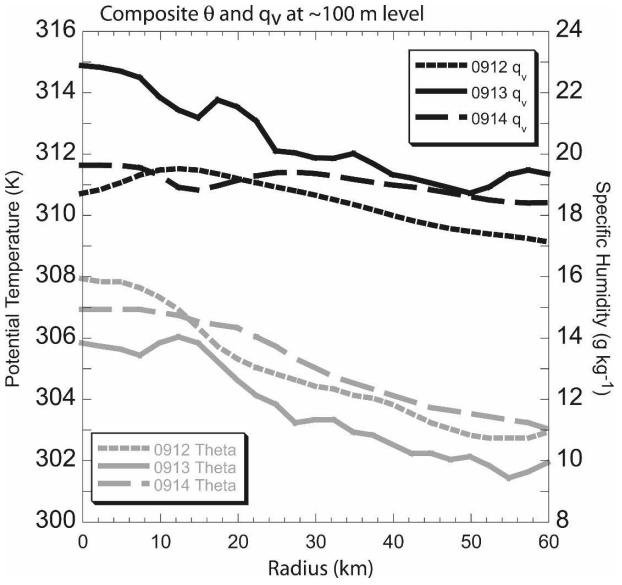

FIG. 6. Azimuthal mean radial profiles of potential temperature and vapor mixing ratio at the lowest composite level (0–250 m, representative of ~100 m) from 12 to 14 Sep 2003.

ertial stability and Rossby elasticity (Cram et al. 2007) at the eyewall and be enhanced by the moist entropy reservoir in the eye before returning to the eyewall cloud.

A key ingredient to understanding hurricane maximum intensity is the amount of moist entropy a parcel is able to gain in the TC boundary layer. Malkus and Riehl (1960) posited that the entropy gain occurs on the inward spiral from the environment to the eyewall. Conversely, Emanuel (1986) argued that convective downdrafts in the rainbands prevent significant material increase of moist entropy for inflowing parcels, such that most of the gain occurs directly under the eyewall. PM03 explored a third mechanism, in which persistent enthalpy fluxes in the low-level eye provide an important additional source of moist entropy for the hurricane engine. As a proxy for the Lagrangian change in θ_e for a boundary layer air parcel, the observed values were averaged over the lowest kilometer in radial bins corresponding to the outer core, eyewall (at the RMW), and eye. These values are shown in Table 1. The outer-core values of mean boundary layer θ_e were similar for each IOP (~350–352 K). This indicates that the gain in θ_e for a hypothetical inflowing air parcel in the boundary layer from the outer core to the eyewall was the largest on the 12 September (~11 K) and smallest on 13 September (~4 K). An additional ~4 and ~14 K, respectively, was available for parcels that were able to access the eye, however. Given that the tangential velocity remained nearly steady state, implying that the

TABLE 1. Mean $\delta\theta_e$ between different regions of the storm on the three analysis days. Values are averaged over the lowest kilometer and are relative to values in the outer core (~351 K at ~250-km radius). Eyewall values are from 10-km-wide radial bins at 25, 45, and 50 km, respectively, and eye values are from variable bins inside these radii. These values can be viewed as a proxy for the Lagrangian θ_e increase of a hypothetical inflowing air parcel that either ascends directly in the eyewall or is able to access the eye before being returned to the eyewall.

	Mean $\delta\theta_e$ (outer core − eyewall)	Mean $\delta\theta_e$ (eyewall − eye)	Mean $\delta\theta_e$ (outer core − eye)
12 Sep	11 K	4 K	15 K
13 Sep	4 K	14 K	18 K
14 Sep	6 K	7 K	13 K

frictional dissipation was similar on each day, the required moist entropy to maintain the intensity on the 13th thus most likely originated in the eye. It is also interesting to note that the inner-core SST estimates were the lowest on this day (27.5°C versus 28.5°–29°C; see section 5a), suggesting that the reduced latent heat fluxes underneath the eyewall were compensated for by radial fluxes from the eye. Isabel appears to have settled into an intermediate structure on the 14th, with an ~6-K increase from the outer core to the eyewall and an additional ~7 K into the eye. This analysis suggests that inflowing parcels could potentially gain on average 13–18 K of θ_e on all three days via different thermodynamic pathways.

c. Potential vorticity and absolute vertical vorticity

The axisymmetric dry Rossby–Ertel potential vorticity (PV; Hoskins et al. 1985) was calculated from the composite gradients of axisymmetric tangential velocity and potential temperature in cylindrical coordinates according to the definition

$$\mathrm{PV} = \alpha(\boldsymbol{\zeta}_{\mathrm{abs}}) \cdot \nabla\theta = \alpha\left\{\left[\frac{\partial(r\upsilon)}{r\partial r} + f\right]\frac{\partial\theta}{\partial z} - \frac{\partial\upsilon}{\partial z}\frac{\partial\theta}{\partial r}\right\}, \tag{1}$$

where α denotes the specific volume, $\boldsymbol{\zeta}_{\mathrm{abs}}$ denotes the absolute vorticity vector, f denotes the Coriolis parameter, υ denotes the tangential velocity, and θ denotes the potential temperature. There is only a slight decrease in the vorticity and PV of the vortex each day, as shown in Fig. 7, due to the slowly expanding wind field and weakening of the radial gradient of tangential wind. The composite vertical vorticity is generally positive everywhere in the domain, with the exception of a small area near 10-km radius on 14 September. This is believed to be an artifact of the analysis resulting from the lack of data, large eye, and weak radial gradient of

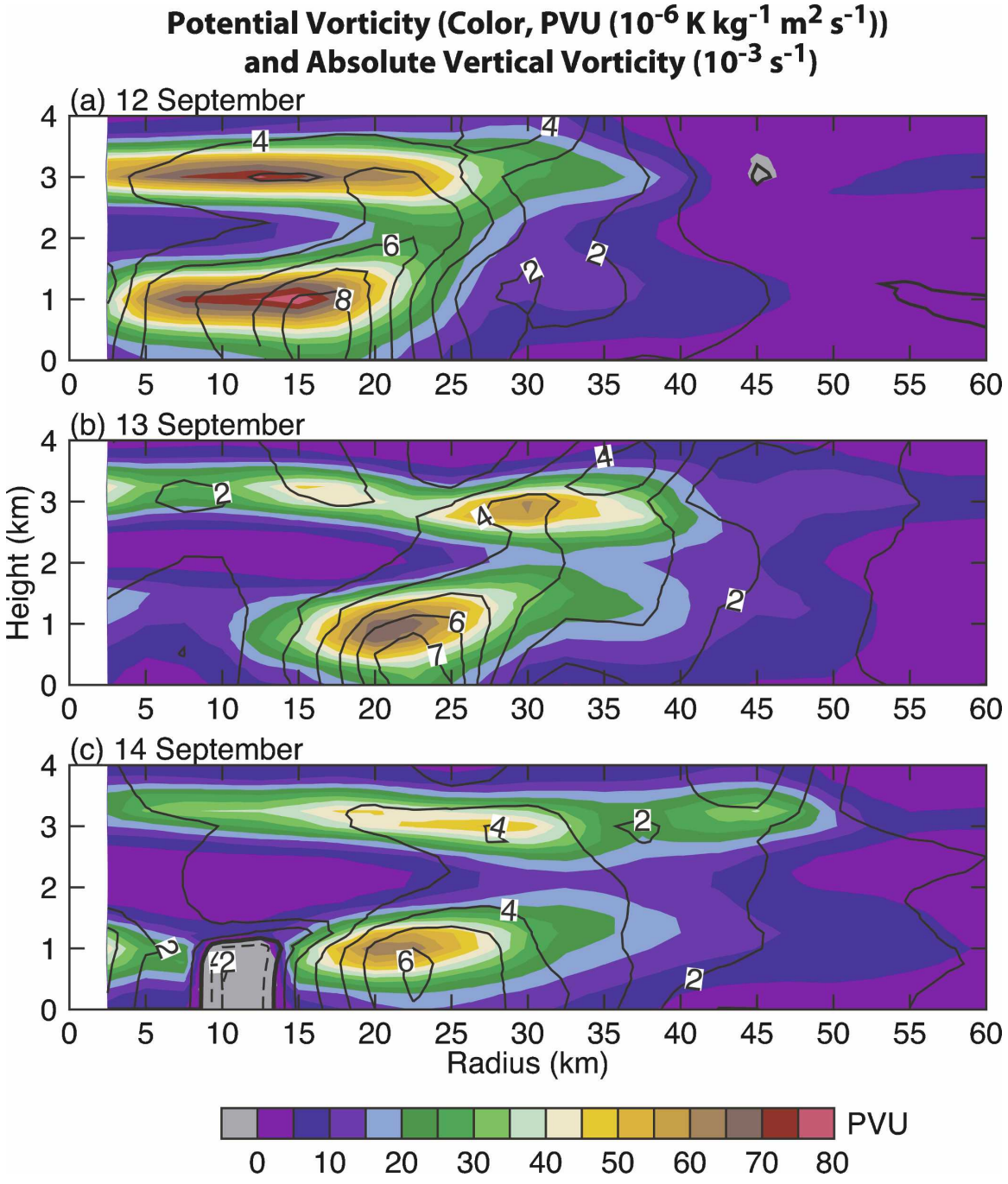

FIG. 7. Radius–height azimuthal mean storm-relative Rossby–Ertel potential vorticity [colors; potential vorticity units (PVU = 10^{-6} K kg^{-1} m^2 s^{-1})] and absolute vertical vorticity (contours; 10^{-3} s^{-1}) from (a) 12, (b) 13, and (c) 14 Sep 2003.

tangential wind in this region. For consistency with the other plots, these data points were left in the final analysis despite the suspect values since the resulting remaining potential vorticity structure was consistent with the other days.

The "hollow tower" or ring structure of PV at ~1-km altitude is clearly evident on all three days, suggesting that the vortex meets the necessary condition for mixed barotropic/baroclinic instability (Montgomery and Shapiro 1995; Schubert et al. 1999). A combined barotropic/baroclinic instability and nonlinear evolution is believed to be responsible for the mesovortices evident in visual satellite (Fig. 2, right column) and photographic images (not shown) of coherent vortex structures in the

eye, polygonal eyewall structures observed by radar (M06, their Fig. 1c), and a smaller-scale eyewall "misocyclone" (Aberson et al. 2006). A detailed stability analysis that includes the presence of moisture is a topic of some interest and will be reported in due course. These mesovortices emerge as the vortex sheet on the inside of the eyewall breaks down. This breakdown process enhances radial mixing and penetration of low-level inflowing air into the eye region (Rotunno 1984; Emanuel 1997; Kossin and Schubert 2001; Montgomery et al. 2002)

There are two regions of high PV evident in Fig. 7: a lower, outer maximum associated with the strong radial shear at the inner edge of the eyewall, and an upper, inner maximum associated with the subsidence inversion in the eye. The eye PV maximum at ~3-km altitude corresponds well to a transition region with a sharp decrease in relative humidity values (not shown), and weak subsidence/near-zero vertical velocity, reminiscent of the tropopause. Inspection of individual dropsonde profiles indicates that the height of the inversion was not homogeneous, although the dataset suggests it was between 2 and 4 km on average. While some of the finescale detail and exact magnitude of the PV fields is most likely dependent on the particular data sampling and compositing technique, the consistent structure inferred on all three days provides confidence that the gross features of this important quantity are effectively captured by this analysis. This structure is qualitatively consistent with full physics numerical simulations (Chen and Yau 2001; Wang and Zhang 2003). The latter study shows a similar feature in the low-level eye of Hurricane Andrew (1992) at ~2.5-km altitude, and the bowl-shaped maximum just inside the RMW typically associated with very intense storms. The variability of the eye thermal inversion and the dynamical role of the PV maximum associated with it are interesting topics for future research.

The PV presented here is the traditional dry Rossby–Ertel PV, calculated by the inner product of the absolute vorticity vector and gradient of potential temperature. It is important to note, however, that part of the simplicity of the EPI framework arises through an assumption of zero moist saturated PV, in which the potential temperature is replaced by saturated equivalent potential temperature (θ_e^*) in Eq. (1). In a zero θ_e^*–PV vortex, lines of constant absolute angular momentum and saturated moist entropy are congruent above the boundary layer, allowing for a PV inversion through knowledge of the boundary conditions alone. In the EPI framework the complete balanced wind and thermal fields can be obtained through knowledge of the radial structure of θ_e in the boundary and outflow layers and the assumption of saturation throughout the hurricane eyewall in the middle troposphere. The above analysis suggests that while the M and θ_e lines are indeed nearly parallel throughout much of the inner core, there are significant deviations from zero θ_e–PV, even in the nearly saturated eyewall, on all three days. These deviations appear most pronounced in the lower troposphere. This is consistent with radial mixing of θ_e and the addition of heat energy from the eye into the eyewall.

4. Assessment of axisymmetric balance

To derive EPI theory, several assumptions about the axisymmetric balance of the tropical cyclone need to be made, including hydrostatic, gradient wind, and thermal wind balance. Before attempting to make predictions using this theory, gradient wind balance is revisited (Willoughby 1990, 1991; Gray 1991) and thermal wind balance, as derived by Kleinschmidt (1951) and Emanuel (1986), is examined here with this high-resolution dataset.

a. Gradient wind balance

The azimuthally averaged radial momentum equation with Boussinesq approximation in cylindrical coordinates is given by

$$-\frac{\partial \overline{p}}{\overline{\rho}\partial r} = \left(-\frac{\overline{v}^2}{r} - f\overline{v}\right) + \frac{D\overline{u}}{Dt} + F, \tag{2}$$

$$F = -(\overline{v'^2})/r + \partial(\overline{ru'^2})/r\partial r + \partial(\overline{u'w'})/\partial z, \quad \text{and} \tag{3}$$

$$D\overline{u}/Dt = \partial\overline{u}/\partial t + \overline{u}\partial\overline{u}/\partial r + \overline{w}\partial\overline{u}/\partial z, \tag{4}$$

where F represents mean eddy flux divergence; $D\overline{u}/Dt$ is the material derivative of the average radial wind; u, v, and w are the cylindrical velocity components; t is time; f the Coriolis parameter (assumed constant); p the total pressure, and ρ the total density. Here, the overbar represents the azimuthal average and primes represent perturbations from the average. If the mean and perturbation wind field is known, Eq. (2) can be integrated radially to obtain the estimated contributions from each term to the overall mean pressure deficit. Here F cannot be determined with the current observations. However, it can be estimated by a residual given the observed pressure gradient and mean flow quantities.

The results of such an integration from composite wind data on 13 September are shown in Fig. 8. The mean wind is assumed steady during the composite period. An inward integration of Eq. (2) using the com-

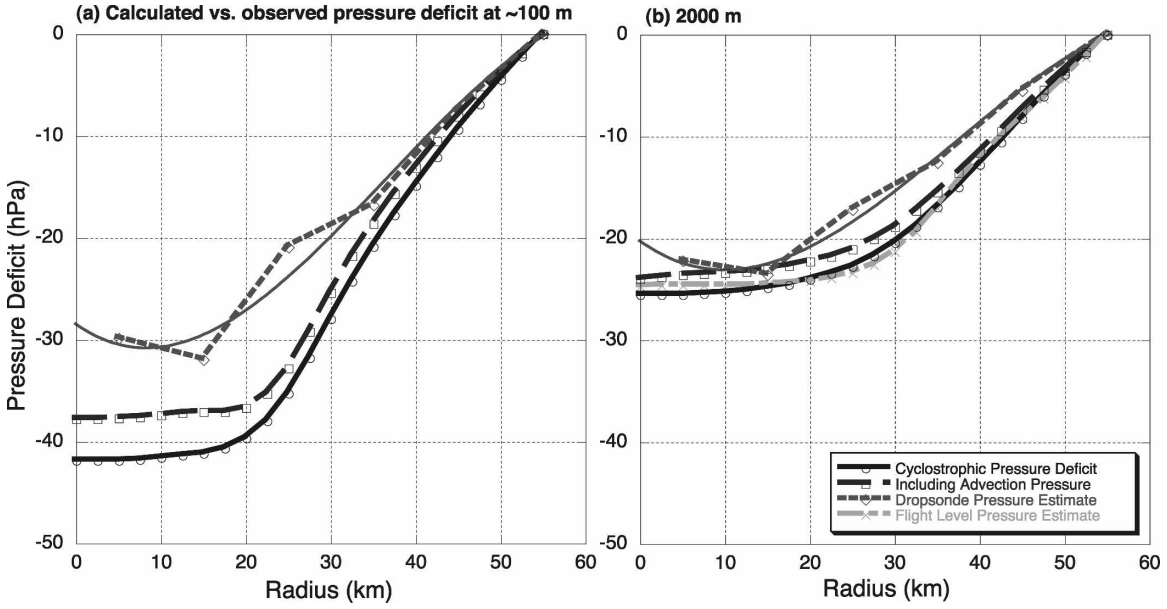

FIG. 8. Calculated pressure deficit obtained by integrating the radial pressure equation [Eq. (4.1)] inward from 55-km radius with (dark gray dashed curve; squares) and without (black solid curve; circles) advection terms vs the pressure deficit observed by dropwindsonde data (light gray dotted curve; diamonds) at (a) 100-m and (b) 2-km altitude. Third-degree polynomial fits (light gray thin curve) of the observed pressure gradient with r^2 values of (a) 0.98 and (b) 0.99 are also shown.

posite mean winds, from 55-km radius with zero as the outer boundary condition, at (a) ~100 m (0–250-m composite level) and (b) 2-km altitude is compared to the observed pressure gradient. The integration was performed with only the cyclostrophic and Coriolis terms (black solid curve) and also including the advection terms ($\overline{u}\partial\overline{u}/\partial r + \overline{w}\partial\overline{u}/\partial z$, gray dashed curve). The observed pressure gradient was calculated in two ways: by averaging dropwindsonde data in 10-km radial and 50-m vertical bins (dotted curve), and from a 1D Barnes analysis of flight-level data at 2 km. The derived pressure field from the 2D Barnes analysis was sensitive to data gaps because of the strong vertical pressure gradient. A 1D Barnes analysis of dropsonde data yields similar results to the binned averages, but underestimated the steep gradient near the inner edge of the eyewall where data were limited.

Figure 8a suggests the importance of the advection terms and the relatively significant contribution from the residual terms in the boundary layer. The transverse advection and eddy flux divergence act together to oppose the cyclostrophic and Coriolis terms and reduce the radial pressure gradient. These terms increase the central pressure by ~6 and ~8 hPa, respectively. While some of the residual may be due to uncertainties in the estimated central pressure, the combined eddy terms are roughly of the same order and sign as the advection terms in the boundary layer. At 2-km altitude, the calculated and observed pressure deficits agree well, consistent with a decrease in radial accelerations and eddy momentum fluxes. Comparisons between the dropsonde and flight-level-derived pressure gradients suggest that both calculations capture the general decreasing trend well, though the binned averaging may slightly underestimate the gradient. Similar results from 12 and 14 September (not shown) suggest that the vortex is roughly in gradient balance above the boundary layer in agreement with prior analyses of other intense storms (e.g., Willoughby 1990).

Alternately, one can calculate the gradient wind from the observed pressure field. The last two terms in (2) are identically zero for a steady-state vortex in pure gradient wind balance, yielding a quadratic equation that can be solved for the gradient wind (V_g) for a given radial pressure distribution. To compute the gradient wind, the binned pressure data was fit to a third-degree polynomial (Figs. 8a,b, thin solid line) and an analytical derivative was obtained. This derivative was then substituted into (2) and solved, yielding a simplified radial profile of the gradient wind (Fig. 9a). While modeling the gradient wind as a quadratic function is clearly an oversimplification, one can still obtain meaningful estimates of super/subgradient winds in Isabel's inner core. From Fig. 9a, the presence of supergradient winds around the eyewall region ($r > 20$ km) at low levels (~100 m) is consistent with the inward deceleration of

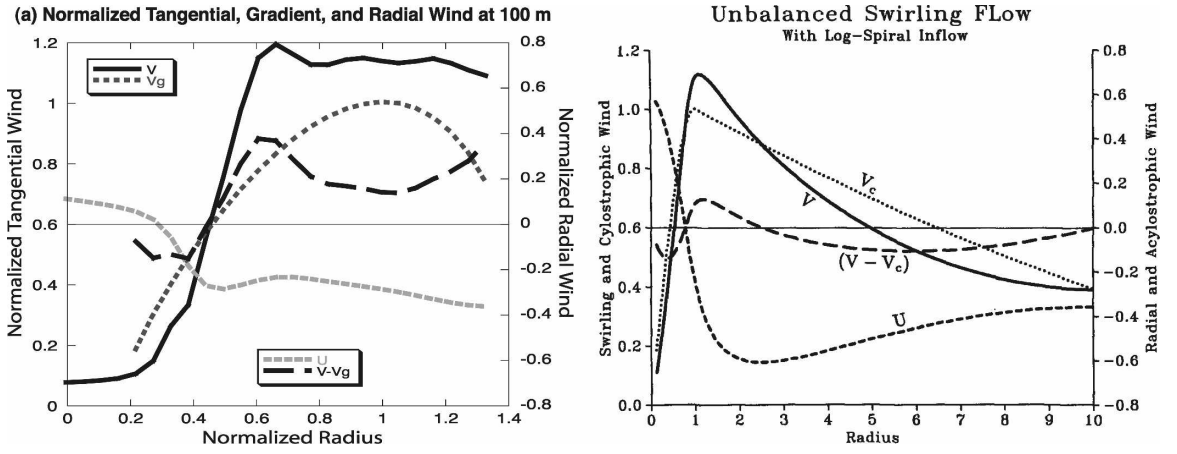

FIG. 9. (a) Composite wind at ~100 m (0–250-m composite level) from Hurricane Isabel on 13 Sep, and (b) calculated nonbalanced wind in a cyclostrophic vortex with specified inflow angle such that the radial wind converges asymptotically to 0.8 times the radius of maximum cyclostrophic wind (from Willoughby 1990). The dotted curve represents the cyclostrophic, or gradient wind; the solid curve the nonbalanced tangential wind; the shorter dashed curve the radial wind; and the longer dashed curve the difference between the balanced and nonbalanced wind. Wind components are nondimensionalized with the maximum balanced wind, and radius is nondimensionalized with the radius of maximum balanced wind.

the radial flow (Smith 1980). Although the simple quadratic function falls off too rapidly at outer radii, it suggests that the boundary layer tangential wind was ~15% supergradient near the RMW.

The transition from super- to subgradient winds occurs at ~20-km radius and is concurrent with a reverse in the radial acceleration near the center of the eye. This pattern is similar to a simple hurricane boundary layer model constructed in Willoughby (1990), shown in Fig. 9b. Willoughby's model used a simple log-spiral inflow to model the radial wind, but the predicted wind structure near the RMW is qualitatively similar to the results from Isabel. The radial acceleration acts effectively like an extra pressure, decelerating the tangential wind in the eye and accelerating it in the eyewall. This analysis is also qualitatively similar to the analytical model presented in Kepert (2001), with the top of the inflow layer coinciding with the location of maximum tangential winds and a supergradient jet below. The results are similar on the other two analysis days (not shown).

b. Thermal wind balance

An assessment of thermal wind balance near the RMW at the boundary layer top was presented in M06 for 13 September. As shown in section 4a, the assumptions made in that paper regarding cyclostrophic balance are reasonably satisfied for Isabel above the boundary layer. The diagnostic thermal wind equation relating the maximum mean tangential wind and the radial gradient of moist entropy at the top of the boundary layer[5] derived by Emanuel [1986, Eq. (13); 1997, Eq. (13)] is repeated here for completeness:

$$V_m^2 \approx -r_m(T_B - T_O)\frac{dS_B}{dr}, \tag{5}$$

where S_B is the moist entropy at the boundary layer top, r is the radius from the vortex center, r_m is the RMW, V_m is the maximum mean tangential wind, T_B is the temperature at the boundary layer top, and T_O is the outflow temperature.

Similar calculations as to the degree of thermal wind balance on 12 and 14 September have been performed here. The results from all three days are summarized in Table 2. There is fair agreement between the observed quantities on the 13th as shown in M06. On the 14th, the entropy gradient appears too weak for the observed tangential wind and outflow temperature. The discrepancy in the radial θ_e gradient of ~1 K (10 km)$^{-1}$ is within the range of uncertainty for this measurement and the sensitivity to this slight discrepancy on this day yields either a 30-K decrease in outflow temperature, or a 10 m s^{-1} decrease in the tangential wind for exact axisymmetric thermal wind balance. A more distinct

[5] This theoretical thermal wind relationship is strictly valid at the height of the maximum wind at the RMW. From Fig. 4, the top of the inflow layer and the height of the maximum wind are at approximately the same level near the RMW on all three days. This altitude is therefore defined as the boundary layer top following Montgomery et al. (2001). Mixed-layer depths for virtual potential temperature were much shallower (~150 m), however, as shown in M06.

TABLE 2. Results of thermal wind diagnostic from Eq. (5) for 12–14 Sep. Top row and first column values are observed quantities. Cell contents in boldface show the results of calculating for the remaining parameter assuming the other two quantities are known.

12 Sep, 25-km RMW V_m = 80 m s^{-1} T_O = −65°C	T_O = −65°C **$d\theta e/dr$ = −10.2 K (10 km)$^{-1}$**	$d\theta_e/dr$ = −5 K (10 km)$^{-1}$ ***T_O = −158°C*** **V_m = 56 m s^{-1}**
13 Sep, 45-km RMW V_m = 76 m s^{-1} T_O = −58°C	T_O = −58°C **$d\theta e/dr$ = −5.7 K (10 km)$^{-1}$**	$d\theta_e/dr$ = −6 K (10 km)$^{-1}$ **T_O = −57°C** **V_m = 74 m s^{-1}**
14 Sep, 50-km RMW V_m = 74 m s^{-1} T_O = −56°C	T_O = −56°C **$d\theta e/dr$ = −4.7 K (10 km)$^{-1}$**	$d\theta_e/dr$ = −3.5 K (10 km)$^{-1}$ **T_O = −83°C** **V_m = 64 m s^{-1}**

discrepancy between the wind and entropy fields at the RMW on 12 September is evident. Because of uncertainties in the inferred radial entropy gradient and calculated outflow temperature (described further in section 5b), it is difficult to assert with confidence that the storm was significantly unbalanced in this regard. The steeper radial entropy gradient near 25-km radius, however, and the apparent consistency at the larger RMW (45 km) on the 13th suggests that some adjustment toward thermal wind balance may have taken place. However, with the limited temporal continuity, the use of pseudoequivalent potential temperature, and the above-mentioned uncertainties, further speculation on the matter is not justified.

5. Potential intensity analysis

A detailed PI analysis of Hurricane Isabel on 13 September was performed in M06, where it was argued that Isabel exceeded the EPI a priori maximum mean tangential wind within the range of 10–35 m s^{-1} on 13 September. The range of values depends on the degree of negative ocean feedback, the numerical value of enthalpy and momentum exchange coefficients at high surface wind speeds, and dissipative heating. Here we continue that analysis with available data from 12 and 14 September. For an EPI prediction of maximum mean tangential wind at the top of the boundary layer, one needs estimates of 1) the SST underneath the hurricane core, 2) the upper-level exhaust (outflow) temperature where parcels undergo radiational cooling to space, 3) the ambient RH near the sea surface, and 4) the ratio of bulk enthalpy to momentum exchange coefficients at high wind speeds. A constant RH of 80% was used in this study as a simple expedient [see Table 3 for ambient RH measurements, and M06 and Camp and Montgomery (2001) for a discussion of this assumption]. The other parameters are examined in the following sections.

a. Sea surface temperature

The average SST over the week prior to Isabel's passage derived from Advanced Very High Resolution Ra-

TABLE 3. Observed and calculated environmental temperatures and RH for Hurricane Isabel from 12 to 14 Sep 2003. RH is the average in the lowest 500 m. Temperature at the boundary layer top (T_B), radial-wind-weighted outflow temperature (T_O RW), equilibrium-level outflow temperature (T_O EL), $d\ln(\theta_e)$-weighted outflow temperature (T_O EPI), and θ_e at the outflow layer top and bottom are also shown.

Sounding	Radius from center (km)	RH (%)	T_B (°C)	T_o RW (°C)	T_o EL (°C)	T_o EPI (°C)	θ_e Bottom (K)	Radial outflow layer: Altitude bottom (m)	Radial outflow layer: θ_e top (K)	Radial outflow layer: Altitude top (m)
TJSJ 2400:00 UTC 12 Sep (SW)	861	82	21.4	−54.5	−58	−64.6	351.7	12 420	363.0	15 030
G-IV 2227:14 UTC 13 Sep (NE)	341	72.6	24.9	−54.2	−59	−52.9	349.7	11 140	358.8	14 060
G-IV 2004:13 UTC 13 Sep (NW)	525	82.5	24.5	−43.4	−44	−54.4	349.7	11 700	354.9	13 210
G-IV 0033:36 UTC 13 Sep (SE)	347	77.7	23.8	−55.7	−50	−56.5	349.8	12 090	359.2	14 359
TJSJ 2400:00 UTC 13 Sep (SW)	584	84.2	24.3	−70.7	−78	−79.5	349.7	14 109	359.2	16 539
Average of 7 soundings on 13 Sep	653.8	80.7	24.1	−52.9	−56.7	−57.8	349.7	12 389	358.0	14 801
G-IV 2004:42 UTC 14 Sep (N)	607	81.0	24.3	−51.2	−47	−56.2	349.8	11 860	357.8	13 470
G-IV 1921:57 UTC 14 Sep (NE)	371	83.9	24.0	−45.8	−52	−51.3	349.7	11 520	357.5	13 290
G-IV 1836:44 UTC 14 Sep (SE)	726	72.9	24.4	−47.1	−48	−61.5	349.7	12 280	359.3	13 770
TJSJ 2400:00 14 Sep (S)	726	71.8	23.2	−39	−61.2	−49.9	349.7	11 079	359.3	14 009
Average of 7 soundings on 14 Sep	609.7	81.9	24	−50.3	−49.4	−55.5	349.8	11 811	356.8	13 417

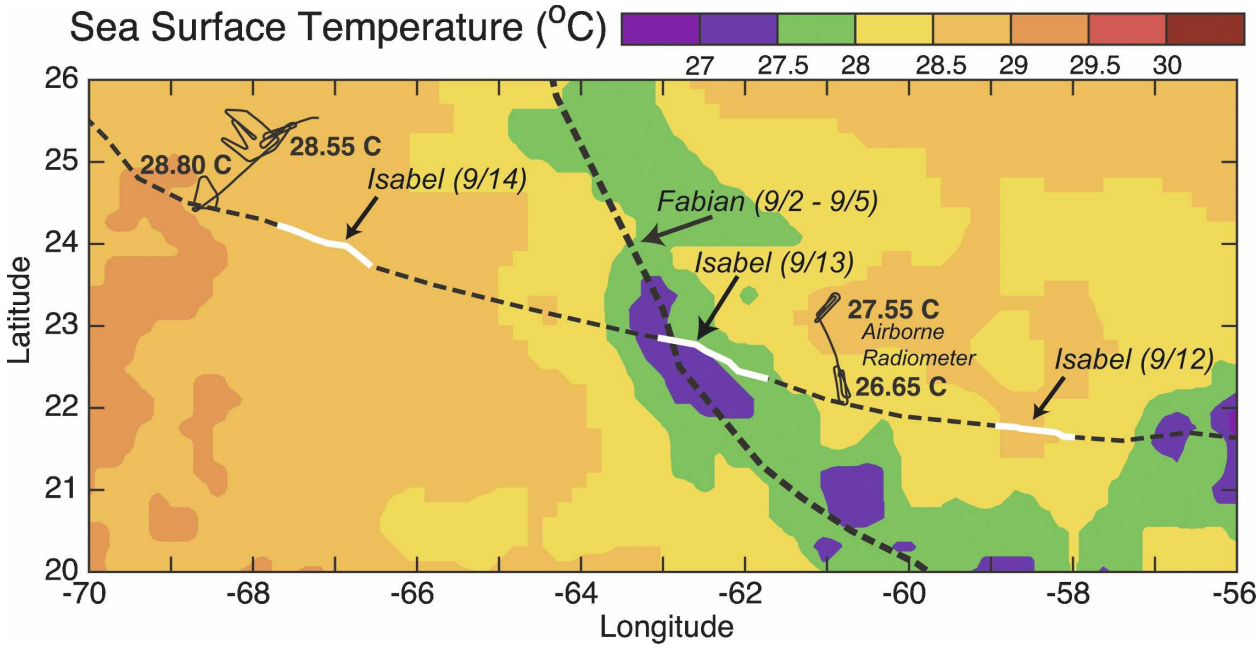

FIG. 10. SST derived from AVHHR satellite (average SST over 4–10 Sep in color) and NOAA WP-3D downward-pointing radiometer (thin line, from ~1800 UTC 13 and 14 Sep). Tracks of Hurricanes Fabian (dashed best track, from 2 to 5 Sep) and Isabel (dashed best track, with thick white, solid line indicating analysis periods from 1600 to 2300 UTC 12–14 Sep) are shown for reference.

diometer (AVHRR) satellite measurements (McMillin and Crosby 1984) is shown in Fig. 10 with the analysis periods highlighted in white. The prestorm satellite-derived temperatures are well validated by airborne radiometer measurements (Moss 1978) recorded on board the P-3 NOAA 43 aircraft at ~60 and ~120 m above sea level to the northwest (in advance) of the storm center on 14 September. Radiometer measurements taken in the rear of Isabel on 13 September measured a reduction in SST by ~1°–2°C relative to satellite-derived SST estimates prior to Isabel's passage. As discussed in M06, this reduction is believed to be caused by shear-induced turbulent upwelling (Price 1981; Shay and Elsberry 1987; Emanuel et al. 2004), an effect that is not included in current EPI theory. Isabel encountered the cool wake of Fabian in the central region of the plot during the IOP on the 13th, and a constant SST of 27.5°C was employed in M06 to represent the average SST for the a priori PI estimates. SSTs on the 12th had values near the inner core of ~28.5°C, and Isabel began to encounter slightly warmer water on the 14th, with the estimated SST near ~29°C.

M06 presented arguments that the maximum sustained tangential wind rapidly adjusts to SST changes underneath the eyewall, consistent with EPI theory. A numerical modeling experiment was performed to test the effect of a cool wake, similar to that experienced by Isabel. This experiment, summarized in the appendix, suggests that the intensity response is on the order of a few hours, and it is therefore likely that Isabel's V_{max} rapidly adjusted to the lower SST.

b. *Outflow temperature*

The outflow temperature was calculated in M06 in three different ways: as a radial-wind-weighted temperature across the storm outflow (PM03); as an equilibrium-level temperature (the temperature at which a virtual parcel starting from ambient surface state achieves the same environmental temperature after lifting by pseudoadiabatic ascent); and as a $d\ln(\theta_e)$-weighted temperature following the original theoretical definition (Emanuel 1986; see M06 for more details relevant to this study). The first approach provides perhaps the most empirical of the three calculations, in that it is a direct measurement of the temperature in the radial outflow of the storm. Its deficiency with observational data is that the outflow is asymmetric and often concentrated in jets (see Fig. 6 of M06; Vladimirov et al. 2001); thus uneven sampling may bias the estimate. The second provides a plausible proxy, in that parcels that rapidly ascend in the eyewall must return to a level of neutral buoyancy as they recede from the storm, cooling gradually and sinking at large distances. The equilibrium level of a particular sounding depends heavily on the surface characteristics; however, it may be biased if these characteristics are significantly differ-

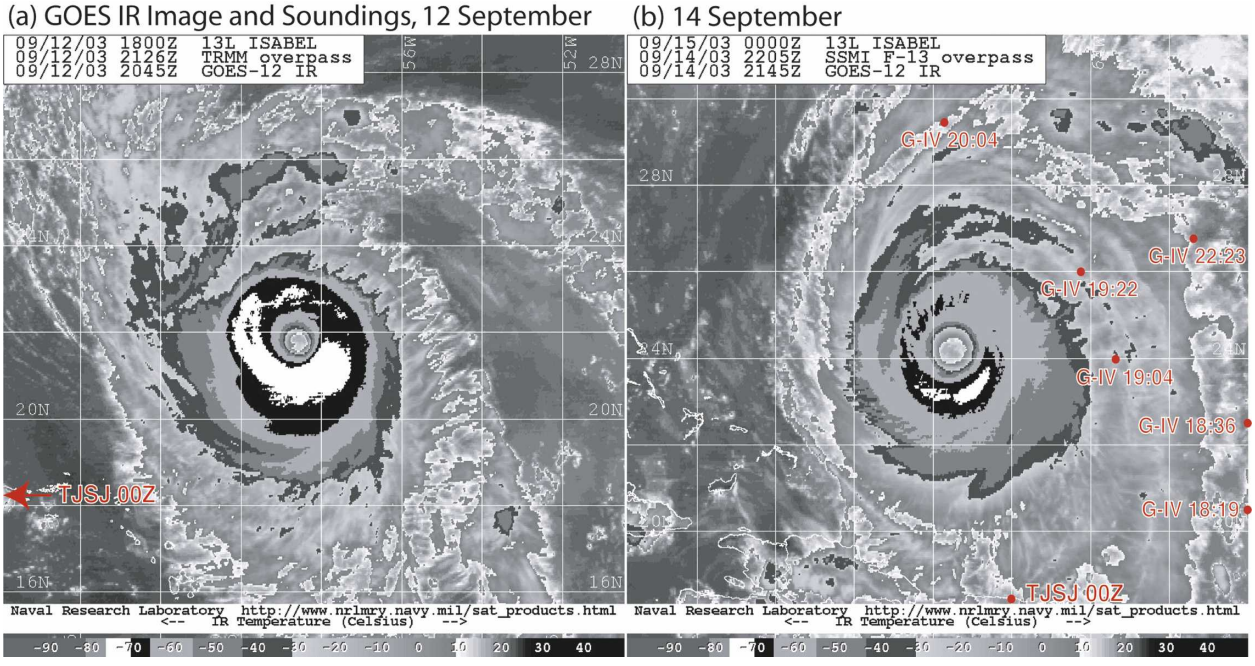

FIG. 11. GOES infrared satellite imagery (courtesy of NRL/Monterey) at (a) 2045 UTC 12 Sep and (b) 2145 UTC 14 Sep showing extent of hurricane outflow, and the dropwindsonde profile locations (red dots with UTC time labels) used in the outflow temperature calculation.

ent than that found in the hurricane environment (i.e., if the sounding was taken over land instead of ocean). The third definition emerges naturally in the EPI formulation, and is based on the "cool reservoir" of the Carnot engine concept. It is the most relevant calculation and forms the primary basis for the outflow temperatures presented here.

The average of seven independently calculated outflow temperatures on 13 September was −58°C and was used as the primary system-scale outflow temperature for that day (see Fig. 6 of M06). Since the NOAA G-IV jet was not deployed on 12 September, a single radiosonde (TJSJ) from San Juan, Puerto Rico, provides the only in situ estimate of the outflow temperature on that day. The San Juan sounding appeared to be an outlier on the 13th, possibly due to the high tropopause height at low latitude, the high equilibrium level since the rawinsonde was launched from land, and/or the different sensor type from the GPS dropwindsondes. The calculated outflow temperatures from this sounding are shown in the first row of Table 3. In this case, the radial wind weighted outflow (RW) and equilibrium level (EL) temperatures are warmer than the $d\ln(\theta_e)$ weighted temperature (EPI). The EPI temperature of −65°C is reasonable, however, yielding a colder outflow than on the 13th or 14th due to higher θ_e integral limits (columns 7 and 9 in Table 3) determined by the composite mean θ_e in the eyewall. Infrared satellite imagery provides a qualitative validation of this estimate, showing generally colder cloud-top temperatures than on the 13th or 14th, but no pixels below −75°C (Fig. 11). This single estimate results in an additional uncertainty in the a priori maximum mean tangential wind of 3–6 m s^{-1}, depending on the specific assumptions used in the calculation.

On 14 September, G-IV reconnaissance provides a comprehensive look at the ambient environment, allowing for a more robust calculation of the outflow temperature similar to 13 September. The bottom rows of Table 3 show a subset of the seven soundings used to calculate the outflow on this day. The three methods described above yield similar estimates near −56°C. This also consistent with the value calculated on the 13th when the storm had similar thermodynamic structure at the eyewall, and with the apparent decrease in cloud-top heights as seen in Fig. 11.

c. *Bulk enthalpy and momentum exchange coefficients*

The complex nature and behavior of the ocean surface at high wind speeds is one of the least understood aspects of hurricane science. Observations of turbulent fluxes of enthalpy and momentum in the hurricane boundary layer at the highest wind speeds to date (~30 m s^{-1}) were collected during the 2002–04 CBLAST field program. These fluxes were then used to calculate

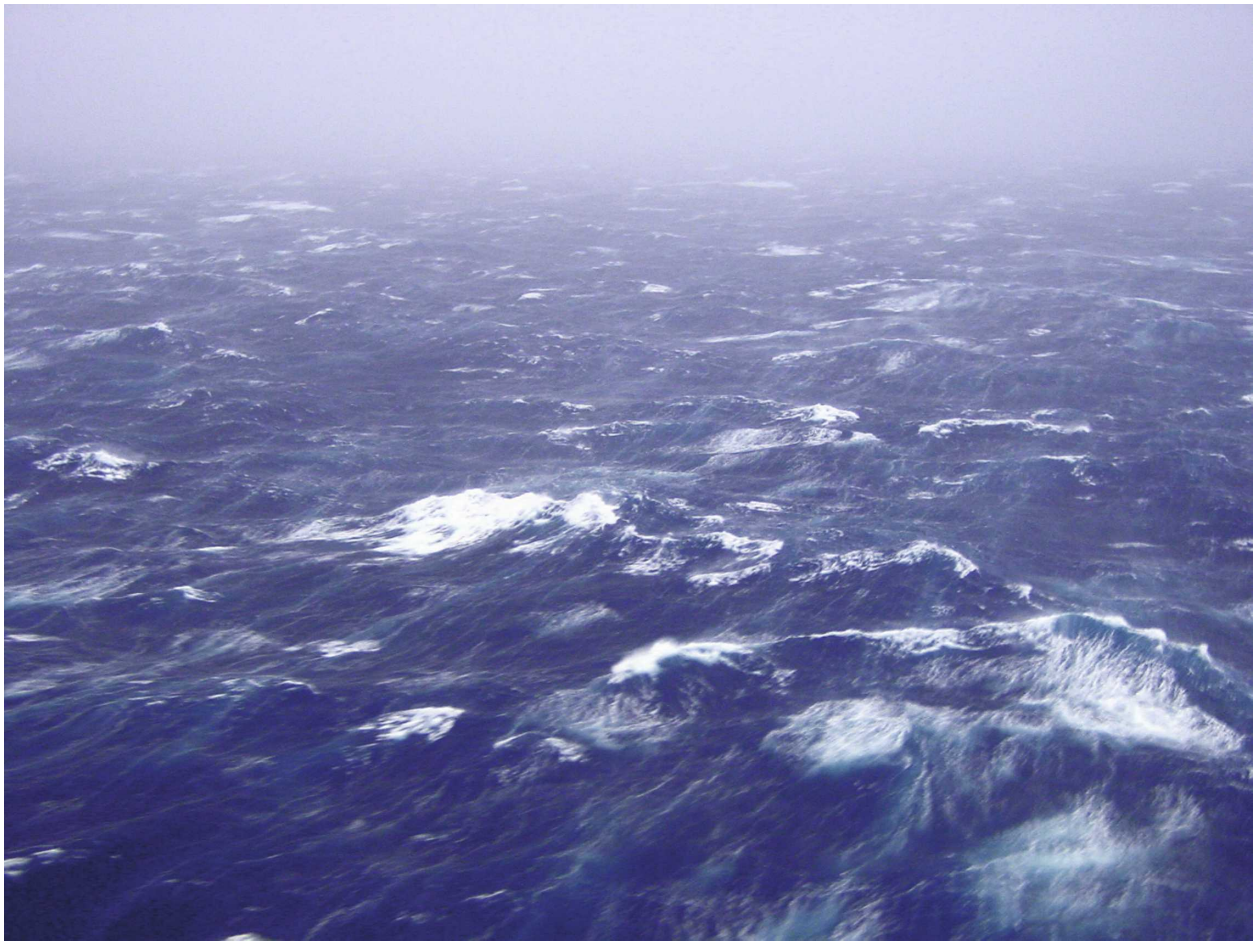

FIG. 12. Photograph of sea surface in Hurricane Isabel taken from NOAA 43 during stepped descent pattern below 400-m altitude. Surface wind speed is 20–30 m s^{-1}. (Photo courtesy of M. Black.)

bulk surface exchange coefficients as a way of parameterizing the air–sea interaction. These results suggest that current estimates of the ratio of exchange coefficients for minimal hurricane-force wind speeds are approximately 0.7 (Black et al. 2007; Drennan et al. 2007; French et al. 2007). Direct measurements were not obtained above these wind speeds, however, because of the inherent difficulty and danger in collecting airborne near-surface measurements at higher wind speeds. A photograph of the sea surface at hurricane-force winds taken during the low-level (~60-m altitude) passes on 13 September is shown in Fig. 12. Wind streaks and waves of varying size and age make parameterizing this complex air–sea interaction challenging, to say the least.

At even higher wind speeds, dropsonde observations (Powell et al. 2003) and laboratory tank experiments by Donelan et al. (2004) suggest that the aerodynamic roughness of the surface, and therefore C_D, reaches a limiting value. Direct observations of the enthalpy flux at extreme wind speeds have not yet been made, but alternative means to determine this coefficient via a budget residual method have been performed using flight-level data (e.g., Hawkins and Imbembo 1976) and are currently underway including dropwindsonde data (K. Emanuel 2005, personal communication). The effects of sea spray on surface fluxes at wind speeds above 30 m s^{-1} are still poorly understood, but likely play an important role in the air–sea interaction in major hurricanes (Fairall et al. 2003). Given these uncertainties, the ratio of bulk enthalpy and momentum exchange coefficients is assumed to be unity ($C_K/C_D = 1$) for the both the upper bound and primary PI estimates in this paper, with a lower bound of 0.5; this range yields an uncertainty in PI of ~20 m s^{-1}.

d. PI estimates: Azimuthal mean V_{max} at boundary layer top

Figure 13 shows the predicted V_{max} from the a priori EPI theory for varying outflow temperatures and near-

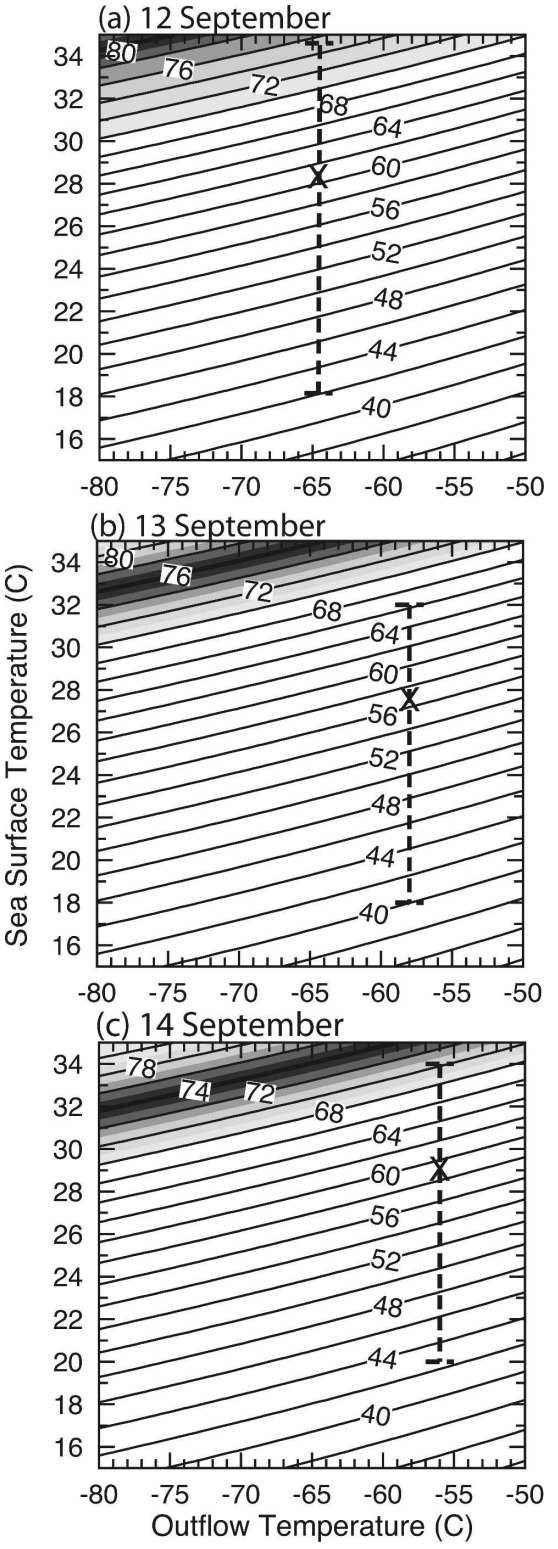

FIG. 13. Theoretically predicted azimuthal mean V_{max} at the boundary layer top for varying outflow temperature and near-core SST with a constant RH = 80%. The "X" indicates the primary potential intensity estimate for the observed near environment around Isabel. The dark solid curve represents the average storm-relative tangential wind speed at the top of the boundary layer derived from the dropwindsonde measurements. The shading represents the standard deviation of this mean value. The a priori EPI estimates assume $C_K/C_D = 1$. See text for assumptions leading to upper and lower bound estimates.

core SSTs with a constant RH = 80%. All calculations were performed using the same assumptions as in M06, where the upper bound for the predicted V_{max} uses a C_K/C_D value of one, assumes a full contribution from dissipative heating (Bister and Emanuel 1998), and assumes no storm-induced ocean cooling (Emanuel et al. 2004). The lower bound assumes a C_K/C_D equal to 0.5, and that dissipative heating is entirely offset by the ocean cooling feedback. The primary estimate compromises these assumptions, with a bulk exchange coefficient ratio of one, and offsetting dissipative heating and ocean cooling. This yields a theoretically predicted 56.6 m s^{-1} EPI for the environmental conditions on 13 September (Fig. 13b), resulting in a 10–35 m s^{-1} discrepancy between theory and observations as Isabel crossed the cool wake of Fabian.

Using these same assumptions one obtains a primary theoretical PI estimate of 61.2 m s^{-1} for 12 September. This value is ~19 m s^{-1} below the observed mean tangential wind at the top of the boundary layer of 80 m s^{-1}. The upper and lower bound estimates yield a range of 42–76 m s^{-1}, including the outflow temperature uncertainty. The highest value is within the standard deviation (10 m s^{-1}) of the mean tangential wind estimate in this case. As was shown in section 4, the boundary layer θ_e structure on 12 September conforms more closely to a more classic (in–up–out) thermodynamic pathway, where substantial θ_e gain is achieved in the outer core and underneath the eyewall. Additional high θ_e in the eye and the presence of eye and eyewall mesovortices (Fig. 3) may be partially responsible for the storm exceeding the a priori PI, however.

Warmer sea surface temperatures yield slightly higher PI values on 14 September than those on 13 September, but weaker than that found on 12 September. Using the same assumptions for the upper and lower bounds yields a range of 42–69 m s^{-1}, with a best estimate of 59.0 m s^{-1}. The PI is therefore exceeded on this day as well, with the maximum value of θ_e in the eye diminished, but the overall area of the potential entropy reservoir was large, similar to the previous day. While the size of the eye likely plays a role in the energetics of the system, it is unknown at this point how much of that energy can be tapped by the hurricane.

6. Conclusions

An analysis of the structure, evolution, and PI of Hurricane Isabel near its maximum intensity was performed using a combination of dropwindsonde, flight-level, satellite, and airborne radar data. The analysis suggests a nearly steady-state intensity, with an expanding tangential wind field accompanied by dramatic changes in the secondary circulation and moist entropy structure. A distinct increase in near-surface radial inflow, eyewall vertical velocity, and low-level θ_e in the eye from 12 to 13 September suggests a buildup of moist entropy due to latent heat fluxes in the relatively quiescent, low-pressure eye, which is then accessed by parcels that are able to penetrate the eyewall, via the intense low-level mean inflow or asymmetric mixing associated with mesovortices. The injection of this heat energy into the eyewall supports the strengthening of the secondary circulation, both in an axisymmetric sense (Shapiro and Willoughby 1982; PM03) and as a local buoyancy source (Braun 2002; Eastin et al. 2005), resulting in, or possibly concurrent with, increased advection of higher momentum air from the outer core and expansion of the wind field. Despite a cooler SST and a rise in central pressure, Isabel maintained 76 $\mathrm{m\,s^{-1}}$ mean tangential winds on 13 September. The storm weakened slightly on 14 September, and exhibited a flattening of the radial entropy gradient in the eyewall region consistent with mixing across the eye–eyewall interface.

The inner-core Rossby–Ertel potential vorticity structure obtained through the Barnes analysis provides a new look at the details of this important dynamical quantity in a category 5 hurricane. Significant absolute vertical vorticity ($>6 \times 10^{-3}\,\mathrm{s^{-1}}$) and PV (>60 PVU) are found radially inward of the eyewall on each day, with a pronounced ring structure typically associated with very intense storms. This ring, or bowl, of high PV supports the necessary condition for combined barotropic/baroclinic instability (Montgomery and Shapiro 1995), which has been shown to be a probable mechanism for producing hurricane mesovortices and polygonal eyewalls (Schubert et al. 1999; Montgomery et al. 2002; Kossin and Schubert 2004). This breakdown of the vortex sheet allows for mixing at the eye–eyewall interface in conjunction with the frictionally driven mean inflow, providing a plausible dynamical pathway for the thermodynamic augmentation of the hurricane engine described in this paper. A secondary PV maximum is found near 3-km altitude in the eye, coupled with a thermal inversion and decrease in relative humidity. This feature has been identified in recent numerical simulations of intense hurricanes (Chen and Yau 2001; Wang and Zhang 2003), but its dynamical significance has not been explored thoroughly to the authors' knowledge. This remains a topic for further research.

An analysis of gradient wind balance on 13 September suggests that the winds in the boundary layer were supergradient in the eyewall region, but transitioned to subgradient inside the eye. This is consistent with the radial accelerations observed in the axisymmetric wind composite, and the inferred radial structure is similar to the simplified log-spiral inflow boundary layer model of Willoughby (1990). At ~100-m altitude, the contribution from the radial advection and eddy/friction terms was significant, opposing the cyclostrophic radial pressure gradient and reducing the central pressure deficit by ~15 hPa. At 2-km altitude, the observed radial pressure gradient and integrated pressure deficit agree well, indicating that the storm was near gradient balance above the boundary layer.

Thermal wind balance was generally difficult to assess using solely the dropwindsonde data because of the diagnostic equation's sensitivity to the radial gradient of moist entropy in the eyewall. Results suggested that the observed moist entropy gradient and outflow temperature were roughly consistent with the maximum mean tangential wind on 13 September, but less so on 14 September. The analysis also revealed a distinct discrepancy on 12 September in the observed radial entropy gradient from that calculated by the thermal wind relationship. The steeper radial entropy gradient at the former RMW (25 km) and the apparent balance at the larger RMW (45 km) by the next day suggest that some adjustment toward thermal wind balance may have taken place, but limited temporal continuity and uncertainty in the entropy gradient and outflow temperature preclude further speculation as to the details of this adjustment process.

We have focused this paper on comparisons with EPI theory since air–sea heat and momentum fluxes are not explicitly included in Miller's (1958) or Holland's (1997) PI theories, nor do these theories offer predictions for V_{max}. This study suggests that Hurricane Isabel's structure and intensity was largely consistent with many of the central concepts of the EPI theory regarding boundary layer balance, and the hurricane as a Carnot engine. However, the evidence that Isabel exceeded Emanuel's PI formulation indicates that revisions to this important dynamical concept need to be addressed. This study provides further evidence that entropy production inside the RMW in the low-level eye provides an active role in hurricane intensification, serving as an important and overlooked energy source for the hurricane engine, and challenges classic theories about the

degree of moist entropy obtained from the ocean in the outer core and underneath the eyewall.

While the conclusions presented here appear robust for this dataset, further research with additional case studies and numerical modeling is needed to elucidate the various thermodynamic pathways available to the tropical cyclone for maintenance and growth. The relative importance of the size of the eye, the amount of eye θ_e that is utilized by the hurricane via injection into the eyewall cloud, and the how important the mechanisms described in this paper may be in weaker storms are interesting and open questions for future research.

Acknowledgments. Special thanks are given to Michael Black and Sim Aberson for their assistance and comments on this research. We acknowledge NOAA/NESDIS for their support of the Ocean Winds Experiment and Hurricane Field Program, NOAA and ONR (Simon Chang) for supporting the CBLAST experiment, and the pilots and support crew of the NOAA-P3 and U.S. Air Force aircraft for their bravery and dedication to hurricane science and forecasting. Dropwindsonde data were processed by Krystal Valde, Bill Ramstrom, and Stephen Feuer. Numerical experiment in the appendix was performed by John Persing. Thanks also are given to Pete Black, Frank Marks, Kerry Emanuel, Roger Smith, and an anonymous reviewer for constructive comments. This research was funded in part by ONR Grant N00014-02-1-0474, and NSF Grants NSF-ATM-0132006, NSF-ATM-0101781, and NSF-ATM-0649946.

APPENDIX

The V_{max} Response to SST Change

The scaling argument offered in footnote 1 of M06 and dynamical considerations based on the intrinsic atmospheric time scales near the RMW of an intense vortex would both suggest that the adjustment time for V_{max} due to a reduced SST around the eyewall region should be rapid (on the order of a few hours). To test this hypothesis we asked Dr. John Persing to assist us by performing two experiments using the axisymmetric Rotunno and Emanuel (1987) numerical model at the "4x" resolution detailed in PM03 with a modified sounding. The two experiments were a control run (CTL) using an SST of 26.1°C and a sensitivity experiment (EXP) with an SST lowered by 1°C within 60 km from the vortex center after 6.5 simulation days when the control experiment had attained a quasi-steady tangential velocity time series (not shown). The 120-km-diameter disk of lower SST is a simple way of mimicking the passage of Isabel over Fabian's wake during the observation period.

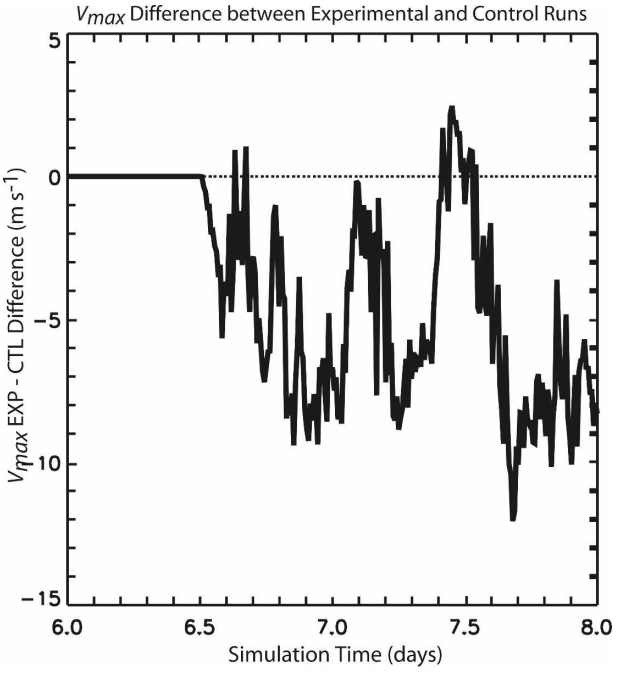

FIG. A1. Difference in the maximum tangential wind (V_{max}) between the experimental run (EXP) and control run (CTL) over time of the axisymmetric hurricane model described in PM03 and Rotunno and Emanuel (1987). The EXP run imposes 1°C SST reduction underneath the eyewall at 6.5 days into the simulation to mimic the passage over a cool hurricane wake.

The outcome of these two experiments is summarized in Fig. A1, which displays the difference between the control and sensitivity experiment of the maximum tangential velocity (in meters per second) as a function of time (in days). As expected, before 6.5 days simulation time the difference is identically zero. Immediately after the cooling ring is imposed in the model, however, the difference plot shows a rapid and nearly linear decrease in V_{max} of several meters per second in approximately 2 h. EPI theory predicts an approximately 2 m s^{-1} decrease per 1°C decrease near the RMW (see Fig. A1). Although this simulated temporary weakening is stronger than predicted using steady-state theory, the main point here is that V_{max} adjusts nearly instantaneously in the direction of the imposed SST change.

On longer time scales, the intrinsic variability between the two runs does manifest itself and it is not yet clear to us how much of this is due to the intrinsic chaos of an intense hurricane vortex and model numerics. Although the difference plot does show that the vortex temporarily rebounds from this local decrease in SST on a time scale of 1.5 days, only the early time tendency is pertinent to the crossing of Fabian's wake. These numerical simulations support the hypothesis that V_{max}

responds to the lowered SST surrounding the eyewall region on a relatively short (hourly) time scale and that V_{max} is not controlled by the SST in the outer region of the storm.

REFERENCES

Aberson, S. D., M. T. Montgomery, M. Bell, and M. Black, 2006: Hurricane Isabel (2003): New insights into the physics of intense storms. Part II: Extreme localized wind. *Bull. Amer. Meteor. Soc.,* **87,** 1349–1354.

Barnes, S. L., 1973: Mesoscale objective analysis using weighted time-series observations. NOAA Tech. Memo. ERL NSSL-62, 60 pp.

Bell, M. M., 2006: Observed structure, evolution, and potential intensity of category five Hurricane Isabel (2003) from 12–14 September. M.S. thesis, Dept. of Atmospheric Science, Colorado State University, 98 pp.

Bister, M., and K. A. Emanuel, 1998: Dissipative heating and hurricane intensity. *Meteor. Atmos. Phys.,* **65,** 233–240.

Black, P. G., and Coauthors, 2007: Air–sea exchange in hurricanes: Synthesis of observations from the coupled boundary layer air–sea transfer experiment. *Bull. Amer. Meteor. Soc.,* **88,** 357–374.

Bolton, D., 1980: The computation of equivalent potential temperature. *Mon. Wea. Rev.,* **108,** 1046–1053.

Braun, S. A., 2002: A cloud-resolving simulation of Hurricane Bob (1991): Storm structure and eyewall buoyancy. *Mon. Wea. Rev.,* **130,** 1573–1592.

Camp, J. P., 1999: Hurricane maximum intensity: Past and present. M.S. thesis, Dept. of Atmospheric Science, Colorado State University, 147 pp.

——, and M. T. Montgomery, 2001: Hurricane maximum intensity: Past and present. *Mon. Wea. Rev.,* **129,** 1704–1717.

Chen, Y., and M. K. Yau, 2001: Spiral bands in a simulated hurricane. Part I: Vortex Rossby wave verification. *J. Atmos. Sci.,* **58,** 2128–2145.

Cram, T. A., J. Persing, M. T. Montgomery, and S. A. Braun, 2007: A Lagrangian trajectory view on transport and mixing processes between the eye, eyewall, and environment using a high-resolution simulation of Hurricane Bonnie (1998). *J. Atmos. Sci.,* **64,** 1835–1856.

DeMaria, M., and J. Kaplan, 1994: Sea surface temperature and the maximum intensity of Atlantic tropical cyclones. *J. Climate,* **7,** 1324–1334.

——, ——, J. A. Knaff, M. Mainelli, and L. K. Shay, 2005: Further improvements to the Statistical Hurricane Intensity Prediction Scheme (SHIPS). *Wea. Forecasting,* **20,** 531–543.

Donelan, M. A., B. K. Haus, N. Reul, W. J. Plant, M. Stiassnie, H. C. Graber, O. B. Brown, and E. S. Saltzman, 2004: On the limiting aerodynamic roughness of the ocean in very strong winds. *Geophys. Res. Lett.,* **31,** L18306, doi:10.1029/2004GL019460.

Drennan, W. M., J. A. Zhang, J. R. French, C. McCormick, and P. G. Black, 2007: Turbulent fluxes in the hurricane boundary layer. Part II: Latent heat flux. *J. Atmos. Sci.,* **64,** 1103–1115.

Eastin, M. D., P. G. Black, and W. M. Gray, 2002: Flight-level instrument wetting errors in hurricanes. Part I: Observations. *Mon. Wea. Rev.,* **130,** 825–841.

——, ——, and ——, 2005: Buoyancy of convective vertical motions in the inner core of intense hurricanes. Part II: Case studies. *Mon. Wea. Rev.,* **133,** 209–227.

Emanuel, K. A., 1986: An air–sea interaction theory for tropical cyclones. Part I: Steady-state maintenance. *J. Atmos. Sci.,* **43,** 585–604.

——, 1988: The maximum intensity of hurricanes. *J. Atmos. Sci.,* **45,** 1143–1155.

——, 1991: The theory of hurricanes. *Annu. Rev. Fluid Mech.,* **23,** 179–196.

——, 1995: Sensitivity of tropical cyclones to surface exchange coefficients and a revised steady-state model incorporating eye dynamics. *J. Atmos. Sci.,* **52,** 3969–3976.

——, 1997: Some aspects of hurricane inner-core dynamics and energetics. *J. Atmos. Sci.,* **54,** 1014–1026.

——, 2005: *Divine Wind: The History and Science of Hurricanes*. Oxford University Press, 285 pp.

——, C. DesAutels, C. Holloway, and R. Korty, 2004: Environmental control of tropical cyclone intensity. *J. Atmos. Sci.,* **61,** 843–858.

Fairall, C. W., E. F. Bradley, J. E. Hare, A. A. Grachev, and J. B. Edson, 2003: Bulk parameterization of air–sea fluxes: Updates and verification for the COARE algorithm. *J. Climate,* **16,** 571–591.

Frank, W. M., 1984: A composite analysis of the core of a mature hurricane. *Mon. Wea. Rev.,* **112,** 2401–2420.

Franklin, J., S. J. Lord, S. E. Feuer, and F. D. Marks Jr., 1993: The kinematic structure of Hurricane Gloria (1985) determined from nested analyses of dropwindsonde and Doppler radar data. *Mon. Wea. Rev.,* **121,** 2433–2451.

——, M. L. Black, and K. Valde, 2003: GPS dropwindsonde wind profiles in hurricanes and their operational implications. *Wea. Forecasting,* **18,** 32–44.

French, J. R., W. M. Drennan, J. A. Zhang, and P. G. Black, 2007: Turbulent fluxes in the hurricane boundary layer. Part I: Momentum flux. *J. Atmos. Sci.,* **64,** 1089–1102.

Gray, W. M., 1991: Comments on "Gradient balance in tropical cyclones." *J. Atmos. Sci.,* **48,** 1201–1208.

Hawkins, H. F., and D. T. Rubsam, 1968: Hurricane Hilda, 1964. II. Structure and budgets of the hurricane on October 1, 1964. *Mon. Wea. Rev.,* **96,** 617–636.

——, and S. M. Imbembo, 1976: The structure of a small, intense hurricane—Inez 1966. *Mon. Wea. Rev.,* **104,** 418–442.

Hobgood, J. S., 2003: Maximum potential intensities of tropical cyclones near Isla Socorro, Mexico. *Wea. Forecasting,* **18,** 1129–1139.

Hock, T. F., and J. L. Franklin, 1999: The NCAR GPS dropwindsonde. *Bull. Amer. Meteor. Soc.,* **80,** 407–420.

Holland, G. J., 1997: The maximum potential intensity of tropical cyclones. *J. Atmos. Sci.,* **54,** 2519–2541.

Hoskins, B. J., M. E. McIntyre, and A. W. Robertson, 1985: On the use and significance of isentropic potential vorticity maps. *Quart. J. Roy. Meteor. Soc.,* **111,** 877–946.

Jorgensen, D. P., 1984: Mesoscale and convective-scale characteristics of mature hurricanes. Part II. Inner core structure of Hurricane Allen (1980). *J. Atmos. Sci.,* **41,** 1287–1311.

Kepert, J., 2001: The dynamics of boundary layer jets within the tropical cyclone core. Part I: Linear theory. *J. Atmos. Sci.,* **58,** 2469–2484.

Kleinschmidt, E., 1951: Grundlagen einer Theorie der tropischen Zyklonen. *Arch. Meteor. Geophys. Bioklimatol.,* **A4,** 53–72.

Koch, S. E., M. DesJardins, and P. J. Kocin, 1983: An interactive Barnes objective map analysis scheme for use with satellite and conventional data. *J. Climate Appl. Meteor.,* **22,** 1487–1503.

Kossin, J. P., and W. H. Schubert, 2001: Mesovortices, polygonal

flow patterns, and rapid pressure falls in hurricane-like vortices. *J. Atmos. Sci.,* **58,** 2196–2209.

——, and ——, 2004: Mesovortices in Hurricane Isabel. *Bull. Amer. Meteor. Soc.,* **85,** 151–153.

Kozich, P., 2006: Inner core structure and intensity change in Hurricane Isabel (2003). M.S. thesis, Rosenstiel School of Marine and Atmospheric Science, University of Miami, 95 pp.

Lawrence, M. B., L. A. Avila, J. L. Beven, J. L. Franklin, R. J. Pasch, and S. R. Stewart, 2005: Atlantic hurricane season of 2003. *Mon. Wea. Rev.,* **133,** 1744–1773.

LeeJoice, R. N., 2000: Hurricane inner-core structure as revealed by GPS dropwindsondes. Colorado State University Department of Atmospheric Science Bluebook 477, 56 pp.

Malkus, J. S., and H. Riehl, 1960: On the dynamics and energy transformations in steady-state hurricanes. *Tellus,* **12,** 1–20.

McMillin, L. M., and D. S. Crosby, 1984: Theory and validation of the multiple window sea surface temperature technique. *J. Geophys. Res.,* **89,** 3655–3661.

Miller, B. I., 1958: On the maximum intensity of hurricanes. *J. Meteor.,* **15,** 184–195.

Montgomery, M. T., and L. J. Shapiro, 1995: Generalized Charney–Stern and Fjortoft theorems for rapidly rotating vortices. *J. Atmos. Sci.,* **52,** 1829–1833.

——, H. D. Snell, and Z. Yang, 2001: Axisymmetric spindown dynamics of hurricane-like vortices. *J. Atmos. Sci.,* **58,** 421–435.

——, V. A. Vladimirov, and P. V. Denissenko, 2002: An experimental study on hurricane mesovortices. *J. Fluid Mech.,* **471,** 1–32.

——, M. M. Bell, S. D. Aberson, and M. Black, 2006: Hurricane Isabel (2003): New insights into the physics of intense storms. Part I: Mean vortex structure and maximum intensity estimates. *Bull. Amer. Meteor. Soc.,* **87,** 1335–1347.

Moss, M. S., 1978: Low-layer features of two limited-area hurricane regimes. NOAA Tech. Rep. ERL NHEML-1, 47 pp.

Persing, J., and M. T. Montgomery, 2003: Hurricane superintensity. *J. Atmos. Sci.,* **60,** 2349–2371.

Pielke, R. A., Jr., and C. W. Landsea, 1998: Normalized hurricane damages in the United States: 1925–95. *Wea. Forecasting,* **13,** 621–631.

Powell, M. D., P. J. Vickery, and T. Reinhold, 2003: Reduced drag coefficient for high wind speeds in tropical cyclones. *Nature,* **422,** 279–283.

Price, J. F., 1981: Upper ocean response to a hurricane. *J. Phys. Oceanogr.,* **11,** 153–175.

Reasor, P. D., M. T. Montgomery, F. D. Marks Jr., and J. F. Gamache, 2000: Low-wavenumber structure and evolution of the hurricane inner core observed by airborne dual-Doppler radar. *Mon. Wea. Rev.,* **128,** 1653–1680.

Rotunno, R., 1984: An investigation of a three-dimensional asymmetric vortex. *J. Atmos. Sci.,* **41,** 283–298.

——, and K. A. Emanuel, 1987: An air–sea interaction theory for tropical cyclones. Part II: Evolutionary study using a nonhydrostatic axisymmmetric numerical model. *J. Atmos. Sci.,* **44,** 542–561.

Schubert, W. H., M. T. Montgomery, R. K. Taft, T. A. Guinn, S. R. Fulton, J. P. Kossin, and J. P. Edwards, 1999: Polygonal eyewalls, asymmetric eye contraction, and potential vorticity mixing in hurricanes. *J. Atmos. Sci.,* **56,** 1197–1223.

Shapiro, L. J., and H. E. Willoughby, 1982: The response of balanced hurricanes to local sources of heat and momentum. *J. Atmos. Sci.,* **39,** 378–394.

——, and M. T. Montgomery, 1993: A three-dimensional balance theory for rapidly rotating vortices. *J. Atmos. Sci.,* **50,** 3322–3335.

Shay, L. K., and R. L. Elsberry, 1987: Near-inertial ocean current response to Hurricane Frederic. *J. Phys. Oceanogr.,* **17,** 1249–1269.

Smith, R. K., 1980: Tropical cyclone eye dynamics. *J. Atmos. Sci.,* **37,** 1227–1232.

——, M. T. Montgomery, and H. Zhu, 2005: Buoyancy in tropical cyclones and other rapidly rotating atmospheric vortices. *Dyn. Atmos. Oceans,* **40,** 189–208.

Tonkin, H., G. J. Holland, N. Holbrook, and A. Henderson-Sellers, 2000: An evaluation of thermodynamic estimates of climatological maximum potential tropical cyclone intensity. *Mon. Wea. Rev.,* **128,** 746–762.

Velden, C. S., C. M. Hayden, W. P. Menzel, J. L. Franklin, and J. S. Lynch, 1992: The impact of satellite-derived winds on numerical hurricane track forecasting. *Wea. Forecasting,* **7,** 107–118.

Vladimirov, V. A., V. I. Yudovich, M. Yu Zhukov, and P. V. Denissenko, 2001: Asymmetric flows induced by a rotating body in a thin layer. HIMSA Preprint 3, Hull Institute for Mathematical Sciences and Applications, 45 pp.

Wang, J., 2005: Evaluation of the dropsonde humidity sensor using data from DYCOMS-II and IHOP_2002. *J. Atmos. Oceanic Technol.,* **22,** 247–257.

Wang, X., and D.-L. Zhang, 2003: Potential vorticity diagnosis of a simulated hurricane. Part I: Formulation and quasi-balanced flow. *J. Atmos. Sci.,* **60,** 1593–1607.

Willoughby, H. E., 1990: Gradient balance in tropical cyclones. *J. Atmos. Sci.,* **47,** 265–274.

——, 1991: Reply. *J. Atmos. Sci.,* **48,** 1209–1212.

——, and M. B. Chelmow, 1982: Objective determination of hurricane tracks from aircraft observations. *Mon. Wea. Rev.,* **110,** 1298–1305.

Zipser, E. J., R. J. Meitin, and M. A. LeMone, 1981: Mesoscale motion fields associated with a slowly moving GATE convective band. *J. Atmos. Sci.,* **38,** 1725–1750.